Murine Alveolar Macrophages Rapidly Accumulate Intranasally Administered SARS-CoV-2 Spike Protein leading to Neutrophil Recruitment and Damage

Authors: Chung Park[1], Il-Young Hwang[1], Serena Li-Sue Yan[1], Sinmanus Vimonpatranon [2,3], Danlan Wei[2], Don Van Ryk[2], Claudia Cicala[2], James Arthos[2] and John H. Kehrl [1,4]

Affiliations:

[1]B-cell Molecular Immunology Section, Laboratory of Immunoregulation, National Institutes of Allergy and Infectious Diseases, National Institutes of Health, Bethesda, Maryland 20892.

[2]Immunopathogenesis Section, Laboratory of Immunoregulation, National Institute of Allergy and Infectious Diseases, Bethesda, Maryland, United States of America.

[3]Department of Retrovirology, Armed Forces Research Institute of Medical Sciences – United States Component, Bangkok, Thailand

[4]Corresponding author.

Running title: Imaging SARS-CoV-2 spike protein in vivo

To whom correspondence should be addressed: John H. Kehrl, Laboratory of Immunoregulation, National Institute of Allergy and Infectious Diseases, National Institutes of Health, Bldg. 10, Room 6A01, 10 Center Dr. MSC 1876, Bethesda, Maryland 20892, United States of America; Fax: 301-402-0070. E-mail: jkehrl@niaid.nih.gov

Keywords: alveolar macrophage, SARS-CoV-2, neutrophil, NETosis, Spike protein, Siglec

Abstract: The trimeric SARS-CoV-2 Spike protein mediates viral attachment facilitating cell entry. Most COVID-19 vaccines direct mammalian cells to express the Spike protein or deliver it directly via inoculation to engender a protective immune response. The trafficking and cellular tropism of the Spike protein *in vivo* and its impact on immune cells remains incompletely elucidated. In this study we inoculated mice intranasally, intravenously, and subcutaneously with fluorescently labeled recombinant SARS-CoV-2 Spike protein. Using flow cytometry and imaging techniques we analyzed its localization, immune cell tropism, and acute functional impact. Intranasal administration led to rapid lung alveolar macrophage uptake, pulmonary vascular leakage, and neutrophil recruitment and damage. When injected near the inguinal lymph node medullary, but not subcapsular macrophages, captured the protein, while scrotal injection recruited and fragmented neutrophils. Wide-spread endothelial and liver Kupffer cell uptake followed intravenous administration. Human peripheral blood cells B cells, neutrophils, monocytes, and myeloid dendritic cells all efficiently bound Spike protein. Exposure to the Spike protein enhanced neutrophil NETosis and augmented human macrophage TNF-α and IL-6 production. Human and murine immune cells employed C-type lectin receptors and Siglecs to help capture the Spike protein. This study highlights the potential toxicity of the SARS-CoV-2 Spike protein for mammalian cells and illustrates the central role for alveolar macrophage in pathogenic protein uptake.

Introduction

In 2019 a new coronavirus (SARS-CoV-2) was identified as the cause of an epidemic outbreak of an acute respiratory syndrome in Wuhan, China. SARS-CoV-2 used the same cell entry receptor—angiotensin converting enzyme II (ACE2)—as did SARS-CoV-1 (1). The SARS-CoV-2 Spike protein mediates cell entry and is a single-pass transmembrane proteins that forms homotrimers. It has a large N-terminal ectodomain exposed to the exterior, a transmembrane helix, and a short C-terminal tail located within the virus. Each Spike monomer contains two regions termed S1 and S2. In the assembled trimer the S1 regions contain the receptor binding domain while the S2 regions forms a flexible stalk, which mediates membrane fusion between the viral envelope and the host cell membrane (2-4). The S1 region is divided into a N-terminal domain and C-terminal domain, the latter interacts with the target cell ACE2 (5-11). Like other Coronavirus spike proteins SARS-CoV-2 Spike protein is heavily N-linked glycosylated (12, 13) and blocking N- and O-glycans dramatically reduced viral entry (14). The SARS-CoV-2 Spike proteins is activated by host cell proteases that cleave the protein at the S1-S2 boundary and subsequently at the S2' site (15-17). Because Spike proteins are located on the surface of the virus, they are a major antigen targeted by the host immune system (18).

During natural infection host immune cells encounter Spike proteins via several different avenues. First, by direct contact with Spike protein bearing viral particles released from infected cells. Second, although the SARS-CoV-2 virions assemble in intracellular compartments of infected cells, unincorporated Spike proteins can reach the plasma membrane. Infected cells expressing Spike proteins may bind to cellular receptors present on resident or recruited immune cells. Third, extracellular vesicles (EVs) released by virally infected cells can contain Spike proteins. Mass spectrometry and nanoscale flow cytometry demonstrated SARS-CoV-2 Spike protein incorporation into EVs (19). Fourth, Spike proteins are pre-processed during viral assembly utilizing the furin protease cleavage site between the S1 and S2 subunits (17). When the Spike protein adopts a fusion conformation the ACE2 receptor-binding domain separates from the membrane-bound S2 subunit. Soluble S1 subunits shed from infected cells or from the virions *in vivo* may bind to other cells via ACE2 or other binding partners. Intriguingly 60% of the plasma samples from patients with post-acute sequelae of coronavirus disease 2019 (PASC) had detectable levels of Spike protein using an ultrasensitive antigen capture assay (20). Prolonged exposure to Spike protein has been suggested to be responsible for Long-COVID syndrome (21). Humans also encounter SARS-CoV-2 Spike protein via vaccination (22). Serious adverse events following vaccination are rare but include vaccine-induced immune thrombocytopenia and thrombosis; myocarditis and pericarditis; and a variety of autoimmune illnesses (23). Due to waning effectiveness humans require repeated immunizations to maintain immunity and protection against potentially severe disease raising some concerns about the impact of repeated exposure to the SARS-CoV-2 Spike proteins.

To better understand the localization and trafficking of the SARS-CoV-2 Spike protein following administration and perhaps during natural infection we prepared a recombinant SARS-CoV-2 Spike ectodomain stabilized in a prefusion conformation (24). This variant (S-2P) contained two consecutive proline substitutions in the S2 subunit. This double-proline substitution (SARS-CoV-2 S-2P) has allowed the rapid determination of high-resolution cryo-EM structures. Fluorescently labeled SARS-CoV-2 Spike ectodomain, a D614G variant (25-27), a high mannose (14), and de-glycosylated version were injected into mice to characterize cellular uptake; were used to characterize uptake and identify human mononuclear cells that bound these proteins, and to perform functional studies. In some instances, we used viral like particles (VLPs) expressing the full-length Spike protein. Our results identified the *in vivo* cellular tropism of the SARS-CoV-2 Spike proteins, delineated their human mononuclear cell targets, provided insights into their functional effects, thereby, helping afford a basis for understanding their impact on humans.

Results

Preparation of SARS-CoV-2 Spike proteins and VLPs expressing them.

We purified a stabilized exodomain of the original SARS-CoV-2 Spike protein (24) using media conditioned by transfected CHO-S or HEK293F cells. Because of higher yields most experiments used CHO-S derived protein. The strategy for producing the recombinant protein is shown (**Figure S1**). Based on its mobility on size exclusion chromatography the Spike proteins spontaneously formed trimers. Kifunensine treated cultures were used to generate a high mannose version, and PNGase F treated protein generated an N-glycan deficient version, and they will be referred to as such. A D614G mutant of the original Wuhan SARS-CoV-2 Spike protein was also purified. Each of the recombinant proteins was subjected to two rounds of Triton X-114 extraction to remove any residual lipopolysaccharide (28). The N-termini of the recombinant proteins were labeled with Alexa Fluor 488. In some experiments we used viral like particles (VLPs) that expressed the original Wuhan Spike protein. We produced the VLPs using HEK293T cells along with a plasmid encoding the human immunodeficiency GAG protein fused to green fluorescent protein (GFP) and a full-length SARS-CoV-2 Spike protein expression vector. Mice inhaled the Spike protein or the SARS-CoV-2 VLPs, while only the Spike proteins were injected intravenously or subcutaneously.

Inhalation of SARS-CoV-2 Spike proteins and Spike protein expressing VLPs affects the lung cellular composition and architecture.

At various time points after Spike protein or VLP inhalation lungs from mice were processed for confocal microscopy. A Siglec-F antibody identified alveolar macrophages (AMs) while CD169 (Siglec-1) immunostaining delineated a subset of large airway associated macrophages (29). Interstitial and inflammatory macrophages do not express Siglec-F. At 3 hours post inhalation low magnification images

131 of mouse lung sections revealed Spike protein (Trimer) uptake by Siglec-F positive cells. Due to the uneven
132 distribution of the inhaled Spike protein the Siglec-F positive cells in the lower portion of the image lack
133 signal (**Figure 1A**). The Siglec-F positive macrophages located near the bronchial epithelium and in the
134 nearby alveoli initially accumulated the labeled protein **(Figure 1B)**. Even at the 30-minute time point
135 AMs had already accumulated it **(Figure 1C)**. Most of the macrophages that acquired the Spike proteins
136 were Siglec-F positive, lacked CD169 **(Figure 1D)**, but were wheat germ agglutinin positive, a mucin
137 marker **(Figure 1E)**. Repeating the experiment but substituting the Spike protein with VLPs expressing the
138 SARS-CoV-2 Spike protein revealed a similar pattern of uptake by AMs **(Figure 1F)**. Immunostaining
139 with LYVE-1 and CD31 to identify the lymphatic and blood vessel endothelium, respectively, **(Figure 1G)**
140 or with Podoplanin another lymphatic endothelial cell marker **(Figure 1H)** showed the rapid accumulation
141 of the Spike protein bearing VLPs in small and large lymphatic vessels. Within 3 hours of administration
142 of either the VLPs **(Figure 1I)** or the Spike protein (data not shown) areas of alveolar collapse and lung
143 damage were evident.

144 To assess the cellular response to Spike protein inhalation and to delineate the cells that had
145 acquired Spike protein *in vivo* we collected mouse lungs 18 hours post exposure to different SARS-CoV-2
146 Spike protein preparations. Saline inhalation served as a control. Lung fragments were digested, and then
147 pushed through a 40-micron cell strainer. Analysis of the collected cells by flow cytometry revealed that
148 the SARS-CoV-2 Spike protein increased the number of neutrophils, monocytes, and dendritic cells in the
149 lung, but did not affect lymphocyte or eosinophil numbers **(Figure 2A)**. Due to the uneven distribution of
150 the inhaled protein and because of their rapid turnover the neutrophil numbers likely underestimate the local
151 neutrophil recruitment. As the imaging experiments indicated AMs most avidly acquired the Spike protein,
152 some interstitial macrophages also retained it, while only a low percentage of the lung neutrophils and
153 dendritic cells were positive following isolation **(Figure 2B)**. Inhalation of the glycan deficient Spike
154 protein reduced the cellular infiltrate and the percentage of cells that retained the protein. The high mannose
155 Spike protein slightly increased the numbers of neutrophil and macrophages in the lung despite a lower
156 uptake by alveolar and interstitial macrophages. Finally, the D614G mutation reduced the cellular infiltrate
157 compared to the unmutated protein and had a slightly different cell binding profile as a greater percentage
158 of monocytes, eosinophils, and dendritic cells retained it **(Figure 2A, B)**. We also tested whether the
159 addition of human ACE2 affected the cellular uptake of the Spike protein following intranasal
160 administration by comparing wild type and the human ACE2 transgenic mice. While we saw little
161 difference by imaging, we did note some minor changes in the cellular uptake pattern, most notably an
162 increase uptake by AM and decrease by interstitial macrophages **(Figure S2)**.
163

164 **Lung neutrophil recruitment and damage 3 hours post inhalation of the Spike protein.**

165 Next, we tested whether inhalation of the Spike protein altered the lung vasculature permeability by having
166 mice inhale either the SARS-CoV-2 Spike protein or the S1 protein from HCoV-HKU1, which was made
167 as a His tagged protein in HEK293 cells. Subsequently we injected Evans Blue intravenously (30).
168 Inspection of the lungs from the treated mice revealed a strong increase in Evan blue staining, which was
169 most pronounced following inhalation of the SARS-CoV-2 Spike protein. Quantifying the Evans blue dye
170 in the collected lungs confirmed the increase in vasculature permeability **(Figure 3A)**. In lung tissue fixed
171 3 hours after inhalation, SARS-CoV-2 Spike protein bearing Siglec-F positive macrophages are surrounded
172 by neutrophils and neutrophil fragments **(Figure 3B, C)**. Imaging fixed lung tissue from mice that had
173 inhaled saline, SARS-CoV-2 Spike protein, glycan deficient protein, the high mannose protein, and the
174 HCoV-HKU1 S1 subunit recombinant protein revealed enhanced neutrophil recruitment with each of them.
175 The surveyed areas of the SARS-CoV-2 Spike protein inhaled mice had approximately a 10-fold higher
176 neutrophil density when compared to saline treated control mice and 4-fold more than the mice that inhaled
177 the SARS-HKU1 S1 protein **(Figure 3D)**.
178
179 **Neutrophil recruitment and damage in the cremaster muscle following local protein injection, and in**
180 **the liver following intravenous injection**
181 An exteriorized cremaster muscle is commonly used to intravitally image mouse neutrophil transmigration
182 and interstitial motility (31). Within 3hours local IL-1β injection recruits bone marrow neutrophils and
183 leads to their transmigration into the nearby tissue. Neutrophils and platelets can be visualized by co-
184 injecting fluorescently labeled Ly6G and Gp1bβ antibodies, respectively. Local PBS injection and
185 intermittent imaging over a 6-hour time frame revealed occasional blood neutrophil and numerous flowing
186 platelets **(Figure 4A, Video 1)**. Local intrascrotal injection of unlabeled SARS-CoV-2 Spike protein caused
187 a modest recruitment of neutrophils at 4-6 hours post injection **(Figure 4A, Video 1)**. To better assess the
188 long-term effect of the SARS-CoV-2 Spike protein, we co-injected Il-1β and waited until the following day
189 to image. Typically, at 24 hours post Il-1β the inflammatory response is resolving, and the interstitial
190 neutrophil numbers are declining from their peak **(Video 2)**. In contrast, each of the Spike proteins
191 adversely affected neutrophil motility and morphology. Numerous neutrophils and neutrophil fragments
192 localized along the blood vessel walls and were scattered within the interstitium **(Figure 4B, Video 2)**. We
193 did not note any significant difference between the different SARS-CoV-2 Spike protein preparations as
194 each caused neutrophil fragmentation and a decline in mobile neutrophils **(Figure 4C)**.
195 We also assessed the impact of injecting the labeled SARS-CoV-2 protein into the blood on the
196 liver sinusoids using intravital microscopy. Snapshots at three hours post infusion revealed Spike protein
197 outlined liver sinusoid endothelial cells co-localized with the CD31 delineated sinusoid endothelial
198 membranes. Kupffer cells identified by F4-80 immunostaining rapidly acquired large amounts of the

199 infused Spike protein **(Figure S3, Video 3)**. The sinusoids, normally devoid of neutrophils, contained many
200 Ly6G$^+$ neutrophils. However, by 18 hours post infusion the amount of Spike protein outlining the sinusoids
201 had declined as had the Kupffer cell associated material **(Figure S3)**. The neutrophil infiltration had largely
202 resolved suggesting that the inflammatory signals had declined. The origin of the white dots interspersed
203 between the sinusoids is unknown, but they were not present at 3 hours post infusion despite identical
204 imaging conditions. One possibility is that altered vascular permeability had allowed some labeled
205 antibodies to leak into the liver parenchyma. To determine whether other endothelial beds also acquired
206 intravenous administered Spike protein we examined the spleen, heart ventricle, and Peyer's patches. At 3
207 hours post infusion endothelial cells at these three sites had acquired the labelled Spike proteins, most
208 prominently in Peyer's patches **(Figure S4)**. Finally, we intravitally imaged the inguinal lymph node at 3
209 and 18-hour after local injection. Typically, locally injected material rapidly enters nearby afferent
210 lymphatics for delivery to the lymph node where subcapsular sinus macrophages first encounter it (32). If
211 it bypasses these macrophages lymph borne material flows into the lymph node medullary region, where
212 medullary macrophages reside. At both the 3-hour time point (data not shown) and at 18 hours subcapsular
213 macrophages showed little interest in the Spike protein, but medullary macrophages avidly acquired it. In
214 contrast to the liver, we did not detect neutrophil recruitment into the lymph node at either time point after
215 tail base injection.
216
217 **Murine and human neutrophils NETosis following exposure to the SARS-CoV-2 Spike protein**
218 Live cell imaging of lung sections following intranasal inhalation of the Spike protein revealed ongoing
219 neutrophil damage and likely NETosis (**Figure 5A**). Time-lapse images show several disrupted neutrophils
220 near a Siglec-F positive AM along with Spike protein bound to a dying neutrophil. This observation along
221 with the cremaster muscle imaging suggested direct neutrophil toxicity. Furthermore, a previous study had
222 shown Spike protein induced neutrophil NETosis (33). To confirm that the Spike protein can trigger
223 neutrophil NETosis and to compare different Spike protein preparations, we briefly exposed murine bone
224 marrow neutrophils and assessed the % of cells undergoing cell death using a flow-based assay. Exposure
225 to fMLP served as a positive control. The lowest concentration of Spike protein (0.1 μg) tested increased
226 the number of dying neutrophils **(Figure 5B)**. Switching to human neutrophils purified from human
227 peripheral blood, exposure to TNFα, LPS or PMA for 4 hours or overnight reduced their viability as
228 expected. Addition of SARS-CoV2 or the D614G mutant protein (1 μg/ml) decreased their viability at 4
229 hours and more dramatically upon overnight exposure. The high mannose versions of the Spike protein and
230 D614G Spike had a slightly greater toxicity at 4 hours but had a similar impact in the overnight assay
231 **(Figure 5C)**. Finally, we imaged human neutrophils overlaid on SARS-CoV-2 Spike protein treated A549
232 cells, a human lung epithelial cell line. Numerous dying neutrophils could be observed likely undergoing

233 NETosis **(Figure 5D, Video 4)**. These results confirm that the SARS-CoV-2 Spike protein can cause
234 neutrophil damage potentially exacerbating the inflammatory response.
235
236 **Human peripheral blood monocytes, B cells, neutrophils, and dendritic cells bind the SARS-CoV-2**
237 **Spike protein**
238 Next, we assessed human peripheral blood leukocyte binding using the fluorescently labeled Spike protein.
239 Binding assays were performed on ice to avoid endocytosis using Hanks balanced salt solution with added
240 Ca^{2+} and Mn^{2+}, or with EDTA to assess cation dependence. Representative CD4 T cell, B cell, Monocyte,
241 or neutrophil flow patterns using either the Spike protein or the high mannose version are shown **(Figure**
242 **6A)**. The flow cytometry results demonstrated that cations enhanced leukocyte binding particularly so with
243 the high mannose protein. The SARS-CoV2 S1 protein bound better than did the HKU1 S1 protein, most
244 evident with NK cells, neutrophils, monocytes, and dendritic cells **(Figure 6B)**. The SARS-CoV-2 Spike
245 protein bound better than did the S1 protein with B cells, neutrophils, and monocytes exhibiting the best
246 binding. The high mannose protein bound less well to the different leukocyte subsets. Surprisingly CD4 T
247 cells poorly bound each of the proteins, irrespective of the presence or absence of cations.
248
249 **Murine and human cells use Siglecs to help capture the SARS-CoV-2 Spike Protein**
250 Since murine and human leukocytes lack significant ACE2 levels, the major entry receptor for SARS-CoV-
251 1 and -2, they likely use other receptors to capture the Spike proteins. The strong co-localization with
252 Siglec-F expressing murine AMs prompted an examination of the role of Siglec-F and other Siglecs in
253 capturing the Spike proteins. Siglecs are transmembrane proteins that exhibit specificity for sialic acids
254 attached to the terminal portions of cell-surface glycoproteins. Several viruses take advantage of sialic acid-
255 Siglec interactions for cell targeting, spreading, and trans-infection (34-36). Initially, we established a bead
256 assay to assess the binding to SARS-CoV-2 Spike proteins. We coupled the S1 domain protein, the SARS-
257 CoV-2 stabilized Spike protein, or the PNGase F treated Spike protein and reacted the beads with
258 fluorescently labeled antibody or different recombinant proteins. Flow cytometry analysis revealed strong
259 binding of the Spike protein antibody, human ACE2, but not murine ACE2 as expected **(Figure 7A)**. Siglec-
260 F also bound well, while the human Siglec-5 and Siglec-8 bound poorly despite being the structural and
261 functional equivalents of Siglec F, respectively (37). Despite the poor binding to the recombinant human
262 Siglecs in the bead assay, we elected to test them in context of a human cell by expressing them in HEK293
263 cells. We chose HEK293 cells as they exhibited little Spike protein binding. We established ACE2, Siglec-
264 5, Siglec-8, Siglec-5/8, ACE2/Siglec-5, and ACE2/Siglec-8 expressing cell lines **(Figure 7B)**. The ACE2
265 transfected cells behaved as anticipated binding the original Spike protein and even better the D614G
266 version; and binding the S1 protein. The high mannose and glycan deficient Spike proteins did not bind. In

contrast to the bead assay both the Siglec-5 and the Siglec-8 expressing HEK293 cells bound the Spike protein, although less efficiently than did the ACE2 expressing cells. They bound the D614G version less well, and very weakly bound the S1 domain protein. The high mannose and glycan deficient Spike proteins exhibited little binding to the Siglec expressing cells. Co-expression of Siglec-5 and -8 did not improve binding, although the ACE2/Siglec co-expressing cells bound the SARS-CoV-2 Spike protein slightly better than did ACE2 only cells. We also imaged the Siglec-5 expressing HEK293 with labeled protein **(Figure 7C)**. The imaging revealed efficient uptake and Spike protein endocytosis. Co-cultured ACE2 and Siglec-5 expressing cells both captured the Spike protein while HEK293 cells not expressing either protein failed to bind or uptake it **(Figure 7D, Video 5)**. To determine whether Siglec-5 or Siglec-8 could contribute to viral transduction, we produced lentiviral particles expressing the Spike protein from SARS-CoV-2, HKU1, or 229E and attempted to transduce the HEK293 ACE2 expressing cells. Successful transduction resulted in GFP expression, which we quantitated by flow cytometry and only occurred with the lentiviral particles with SARS-CoV-2 Spike protein incorporation **(Figure 7E)**. Both a receptor binding domain antibody and recombinant ACE2 blocked transduction. Recombinant human Siglec-5 partially inhibited although it required relatively high concentrations, while human Siglec-1, human Siglec-2, and murine Siglec-F had no impact on the transduction frequency.

Increased TNF-α and IL-6 production by human macrophages exposed to the SARS-CoV-2 Spike proteins.

Dysregulated cytokine production contributes to the pathogenesis of severe COVID-19 infections (38, 39). To assess whether the Spike proteins can affect macrophage cytokine profiles we cultured human monocytes using conditions that generate M0, M1, or M2 macrophages and treated them with different Spike protein preparations. We collected cell supernatants two days later and measured a panel of known macrophage derived cytokines by ELISA **(Figure 8)**. We found little induction of IL-1β in the cell supernatant indicating that the Spike proteins alone did not trigger the inflammasome activation in these macrophages. In contrast, we did observe significant increases in TNF-α and IL-6 secretion by the original SARS-CoV-2 Spike protein treated macrophages irrespective of whether it was produced in CHO or HEK293 cells. The high mannose protein elicited a similar cytokine profile. The HKU-1 S1 protein did not modify cytokine production by any of the macrophage subsets.

Discussion

This study analyzed the cell tropism of the SARS-CoV-2 Spike protein and some of its variants using fluorescently labeled proteins and mice to assess *in vivo* binding and human peripheral blood to assess human leukocyte binding. The intranasal administration of SARS-CoV-2 Spike protein to mice led to its

301 rapid uptake by Siglec-F positive AMs. The reduced uptake of the high mannose Spike protein suggested
302 that AM receptors that interact with complex glycans mediated a portion of the uptake. We confirmed
303 Siglec-F as a potential capturing receptor, as it efficiently bound to the S1 domain, and the SARS-CoV-2
304 Spike protein. Arguing against a role for mSiglec-1, $CD169^+$ lung macrophages and $CD169^+$ subcapsular
305 sinus macrophages failed to accumulate the Spike protein *in vivo*. The closest human paralog of mouse
306 Siglec-F is hSiglec-8 (40). While expressed on human eosinophils and mast cells, human AMs apparently
307 lack it. In contrast, human AMs do express Siglec-5 (37). Along with its paired receptor, hSiglec-14, Siglec-
308 5 can modulate innate immune responses (41). When tested in a bead binding assay, in contrast to Siglec-
309 F, neither hSiglec-5 or -8 bound the recombinant Spike protein, yet their expression in a cellular context
310 allowed binding. Additionally, recombinant hSiglec-5 partially inhibited the transduction of Spike protein
311 bearing viral like particles into ACE2 expressing HEK293 cells. Evidently the recombinant protein binding
312 assay we employed did not fully capture the properties of hSiglec-5 or hSiglec-8 in a cellular context. A
313 recent study of human lungs revealed scant alveolar ACE2 expression, highlighting the importance of
314 alternative Spike protein receptors (42). *Ex vivo* infected human lungs and COVID-19 autopsy samples
315 showed AMs positive for SARS-CoV-2 and single-cell transcriptomics revealed nonproductive virus
316 uptake, and activation of inflammatory and anti-viral pathways. Another study which analyzed pulmonary
317 cells from COVID-19 patients found that myeloid cell C-type lectin engagement induced a robust
318 proinflammatory responses that correlated with COVID-19 severity (43). The robust Spike binding to AMs
319 and their potential roles in COVID-19 lung infection warrants a further exploration of their Spike protein
320 binding partners.

321 The intranasal administration of the Spike protein resulted in an increase in lung vascular
322 permeability and local tissue damage. While the mechanisms are unknown, infectious agents that target
323 AMs can trigger the secretion of factors that disrupt the integrity of the pulmonary microvascular cell
324 barrier. For example, Porcine reproductive and respiratory syndrome virus infected AMs trigger
325 transcriptional changes in genes in co-cultured microvascular endothelial cells that reduce vascular integrity
326 (44). Lung endothelial cells may also be directly targeted (45). Spike protein/ACE2 interactions reduce
327 endothelial cell ACE2 expression, which can alter vascular permeability. Yet, the low affinity of mouse
328 ACE2 for the SARS-CoV-2 Spike protein presumably precludes this mechanism in this study. Also arguing
329 against a role for ACE2 in our model, the responses to intranasal Spike protein in human ACE2 transgenic
330 mice resembled those of wild type mice. The Spike protein RGD (Arginine-Glycine-Aspartic Acid) motif
331 can also bind $\alpha_V\beta_3$ integrins present on endothelial cells (46). This affects VE-cadherin function and
332 vascular integrity. However, we did not detect any Spike protein on the pulmonary blood vessels following
333 intranasal administration although a low level of binding may have escaped visualization. In sum, the rapid
334 and intense uptake of Spike protein by AMs supports a role for these cells in the localized neutrophil

335 recruitment, nearby tissue damage, and increased vascular permeability that follows its intranasal
336 administration.

337 The intravenous administration of the Spike protein, led to its accumulation by Kupffer cells in the
338 mouse liver. This uptake was accompanied by a transitory increase in liver sinusoid neutrophils. Human
339 Kupffer cells express LSECtin (liver Siglec and lymph node sinusoidal endothelial cell C-type lectin,
340 CLEC4G) a C-type lectin receptor encoded within the L-SIGN/DC-SIGN/CD23 gene cluster. LSECtin acts
341 as a pathogen attachment factor for Ebola virus and the SARS coronaviruses suggesting that it contributed
342 to the Kupffer cell uptake we noted (47). The liver sinusoid endothelial cells also avidly accumulated the
343 Spike protein. These cells express another C-type lectin receptor L-SIGN (CD209L/CLEC4M), which has
344 been shown to interact in a Ca^{2+}-dependent manner with high-mannose–type N-glycans on the SARS-CoV-
345 2 Spike protein (48). Based on our mouse studies, blood borne SARS-CoV-2 Spike proteins, viral particles,
346 or exosomes bearing the Spike protein are likely to accumulate in the liver during severe or prolonged
347 COVID-19 infection.

348 Local injection of the Spike protein in the region of the cremaster muscle recruited low numbers of
349 neutrophils, but co-administration with IL-1β caused severe neutrophil damage. The Spike protein also
350 proved toxic to purified mouse and human neutrophils cultured *ex vivo* in its presence. Most human
351 neutrophils bound the recombinant Spike protein. The presence of cations in the binding buffer substantially
352 enhanced the binding suggesting that a cation dependent receptor accounted for a significant portion of the
353 binding. While the high mannose version bound neutrophils less well, in the NETosis assay it produced a
354 similar level of neutrophil cell death. Neutrophils likely employ several different receptors to capture the
355 Spike protein. Human neutrophils express several C-type lectin receptors including CLEC5A, which has
356 been implicated in SARS-CoV-2 triggered neutrophil NETosis (49). They also express Siglec-5 (37), which
357 bound the Spike protein when expressed in HEK293 cells.

358 In this study, inhaled SARS-CoV-2 Spike protein and VLPs bearing the Spike protein rapidly
359 accumulated on AMs. They used Siglec-F and likely other cell surface molecules to capture the Spike
360 protein. Following inhalation, the integrity of the pulmonary vasculature weakened. Resident and recruited
361 neutrophils suffered, either directly targeted by the Spike protein, or secondarily due to the inflammatory
362 response. A similar scenario would be expected during SARS-CoV-2 infection, following direct instillation
363 of the Spike protein in the upper airway of humans, or following an intranasal vaccine that directs the
364 synthesis of the SARS-CoV-2 Spike protein or fragments. Our data indicates that viral particles and soluble
365 Spike protein that spills into the blood during SARS-CoV-2 infection or following immunization will be
366 cleared by liver Kupffer cells but will also target blood vessel endothelial cells. Local delivery of the Spike
367 protein that occurs following vaccination, rapidly delivers the Spike protein to the draining lymph node via
368 afferent lymphatics. Surprisingly, we found that lymph node medullary macrophages, which largely serve

369 a degradative function, uptake the Spike protein. Designing a less toxic Spike protein immunogen that
370 targets subcapsular sinus macrophages might better deliver the immunogen to B cells, thereby eliciting a
371 more efficacious antibody response.
372
373 **Material and Methods**
374
375 **Mice**
376 C57BL/6 and K18-ACE2 transgenic mice were obtained from Jackson Laboratory. All mice were used in
377 this study were 8-12 weeks of age. Mice were housed under specific-pathogen-free conditions. All the
378 animal experiments and protocols used in the study were approved by the NIAID Animal Care and Use
379 Committee (ACUC) at the National Institutes of Health.
380
381 **Cells**
382 To isolate mouse lung cells, lungs were carefully collected and gently teased apart using forceps into RPMI
383 1640 media containing 2 mM L-glutamine, antibiotics (100 IU/ml penicillin, 100 μg/ml streptomycin), 1
384 mM sodium pyruvate, and 50 μM 2-mercaptoethanol, pH 7.2. The tissue was then digested with Liberase
385 Blendzyme 2 (0.2 mg/ml, Roche Applied Science) and DNase I (20 μg/ml) for 1hr at 37°C. The proteases
386 were inactivated by adding 10% fetal bovine serum and 2 mM EDTA and the cell disaggregated by passing
387 them through a 40 μm nylon sieve (BD Bioscience). Single cells were then washed with 1% Bovine serum
388 albumin (BSA) in PBS and blocked with anti-Fcγ receptor (BD Biosciences). Human peripheral blood
389 mononuclear cells (PBMC) were purified from whole blood by density gradient centrifugation (Ficoll-
390 Paque™, Miltenyi Biotec). Whole blood was collected from healthy donors through an NIH Department
391 of Transfusion Medicine (DTM)-approved protocol (Institutional Review Board of the National Institute
392 of Allergy and Infectious Diseases [NIAID]). Neutrophil and monocyte cell population were each obtained
393 by negative selection (>97% purity, Stem Cell Technologies). To generate human monocyte-derived
394 macrophages, purified monocytes were treated for 7 days with 50 ng/ml human recombinant M-CSF
395 (PeproTech) in RPMI medium supplemented with 10% heat inactivated fetal bovine serum, and 1mM
396 Sodium Pyruvate, 100U Penicillin-Streptomycin (Gibco, ThermoFisher Scientific) in ultra-low attachment
397 culture 100mm dishes. On day 7 the mature macrophages were collected and verified to be more than 90%
398 $CD68^+$ by flow cytometry.
399
400 **Reagents**
401 See reagent table.
402

403 **Flow Cytometry**

404 Single cells were re-suspended in 0.1% fatty acid free BSA-Hanks' Balanced Salt Solution (HBSS) with
405 100 μM CaCl2 and 1 mM MnCl2 unless otherwise specified. Buffer without divalent cations included 10
406 mM EDTA. The cells were stained with fluorochrome-conjugated antibodies against various cell surface
407 markers or with different fluorochrome-conjugated proteins, which are listed in the resource and reagent
408 tables in the supplement. LIVE/DEAD™ Fixable Aqua Dead Cell Stain Kit, LIVE/DEAD™ Fixable Near-
409 IR Dead Cell Stain Kit or LIVE/DEAD™ Fixable Yellow Dead Cell Stain Kit (Thermo Fisher) were used
410 in all experiments to exclude dead cells. Compensation was performed using AbC™ Total Antibody
411 Compensation Bead Kit (Thermo Fisher) and ArCTM Amine Reactive Compensation Bead (Thermo
412 Fisher) individually stained with each fluorochrome. Compensation matrices were calculated with
413 FACSdiva software. Data acquisition included cell number count was done on a FACSCelesta SORP (BD)
414 flow cytometer and analyzed with FlowJo 10.8.x software (Treestar).

415

416 **Human macrophage polarization and cytokine profiling**

417 To polarize human macrophages, monocyte derived macrophages were plated in 48 well plates at 5 x 10^4
418 cells per well in 500μl RPMI medium and allowed to rest 2hours at 37°C before treat of cytokines or LPS.
419 The human M0 macrophages were either left untreated or treated for 48h to induce macrophage
420 polarization: (i) for M1 polarization with 10 ng/mL LPS (E055:B55; Sigma-Aldrich) and 20 ng/mL IFNγ
421 (PeproTech), (ii) for M2 polarization with 50 ng/ml human recombinant M-CSF, 20 ng/ml human
422 recombinant IL-4, and 20 ng/ml human recombinant IL-13 (PeproTech). Human macrophages were then
423 cultured alone or with 0.1ug, or 1ug SARS-CoV-2 Spike proteins for 48 hr. The cultured supernatants were
424 collected, and cytokine levels determined using the bead-based immunoassays LEGENDplex™ Human
425 Macrophage/ Microglia Panel (Biolegend). The assays were performed in 96-well plates following the
426 manufacturer's instructions. For measurements a FACSCelesta SORP flow cytometer (BD Biosciences)
427 was employed, and data were evaluated with the LEGENDplex™ Data Analysis software.

428

429 **Production and purification of recombinant SARS-CoV-2 Spike proteins (see Figure S1)**

430 SARS-CoV-2 spike expression vectors were purchased from SinoBiological (see reagent table). Endotoxin-
431 free plasmids were prepared by Alta Biotech and provided at a concentration is 5mg/mL. Transfections
432 were carried out using CHO Freestyle cells (Invitrogen). 1.24mg of plasmid DNA was transfected into 90
433 million cells were using a MaxCyte Electroporation Transfection System. A detailed protocol is available
434 at https://maxcyte.com/atx. Culture supernatants were harvested on day 6 and clarified by centrifugation,
435 followed by filtration through a 0.45μm filter, followed by the addition of EDTA-free protease inhibitor
436 cocktail tablets (Roche). Culture supernatants were then dialyzed overnight at 4℃ in HBS (150mM NaCl,

437 10mM HEPES, pH 8.0) using 10kDa MWCO Slide-A-Lyzer dialysis cassettes (Thermo Scientific).
438 Supernatants were passed over a 10 ml StrepTrap HP column (Cytiva) at 1 ml/min using an ÄKTA pure
439 150 purifier (Cytiva), maintained at 4°C. Bound protein was eluted with elution buffer (2.5mM
440 desthiobiotin, 100mM Tris-Cl, 150mM NaCl, 1mM EDTA, pH 8.0). Peak fractions were pooled and
441 concentrated using 30kDa MW CO Amicon centrifugal concentrators (Millipore). Trace endotoxins were
442 removed by two sequential Triton X100 extractions, followed by passage through an HiPPR detergent
443 removal column (Thermo Fisher). Protein concentrations were determined by a BCA Protein assay (Thermo
444 Fisher).
445
446 **Viral like particles and lentivirus preparation**
447 SARS-CoV-2 Spike protein incorporated NL4.3-GFP VLPs were produced by transfecting HEK293T cells
448 with full length SARS-CoV-2 Spike-S and HIV-1 NL4-3 Gag-iGFP ΔEnv (12455, NIH AIDS Reagent
449 Program) at a ratio of 1:2.5 using a previously reported method (32). EGFP control lentiviruses (no Spike
450 protein) were produced by transfecting HEK293T cells with pCMV-dR8.2 dvpr (packaging) and
451 pLentipuro3 TO V5-GW EGFP-Firefly Luciferase (reporter). Coronavirus Spike proteins were
452 incorporated by co-transfection with SARS-CoV-2 Spike-S, HCoV-229E Spike, or HCoV-HKU1 Spike
453 expressing plasmids. Eighty percent confluent HEK293T in six well plates (2.5 ml/well) were transfected
454 with 5 µg of plasmid diluted in Opti-MEM with a 1:4 (DNA/reagent) dilution of TransIT-293 Transfection
455 Reagent. The media was harvested 64 hr later and centrifuged at 500 ×g for 10 min at 4 °C. The supernatants
456 were collected and mixed with Lenti-X Concentrator (Takara Bio USA, Inc) at a 1:3 ratio. The mixture was
457 placed at 4 °C overnight and centrifuged the following day at 1500 ×g for 45 min. Fluorescent VLPs were
458 directly counted and measured by BD FACSCelesta™ flow cytometer. The forward scatter (FSC) detector
459 (Photodiode with 488/10 BP filter) and side scatter (SSC) detector (photomultiplier tube (PMT) with 488/10
460 BP filter) were tuned to detect voltages up to 530 for FSC and 220 for SSC. The NL4.3-GFP VLPs were
461 distinguished from noise and non-VLP particles by GFP signals. NL4.3-GFP VLP spike protein
462 incorporation was tested using human ACE2 expressing HEK293 cells (ACE2/HEK293). Ten thousand
463 VLPs were incubated with 1×10^4 ACE2/HEK293 cells in 1× HBSS (contains; 1 mM Ca^{2+}, 2 mM Mg^{2+}, 1
464 mM Mn^{2+} and 0.5% fatty acid free BSA) buffer at 4 °C for 30 min. Binding of the VLPs to ACE2/HEK293
465 cells was measured with BD FACSCelesta™. The 50% lentivirus transduction dose was determined using
466 percentile (50%) of GFP positive ACE2/HEK293 cells 3 days after transduction. The pelleted VLPs or
467 lentiviruses were suspended in PBS and frozen in single use aliquots.
468
469 **Lentivirus transduction assay**

470 96-well plates were seeded with 200 µl of ACE2/HEK293 cells (1.5×10^4 cells/ml). After a 24 h incubation,
471 recombinant proteins or neutralizing antibody was added. Lentiviral particles capable of transducing 50%
472 of the cells (CoV2-lenti, HKU-1-lenti, and 229E-lenti) were added (~25 µl) 30 min later. Following a three-
473 day culture, the ACE2/HEK293 cells were harvested and GFP expression levels determined by BD
474 FACSCelesta™ flow cytometry. Each group contained 2-5 replicates.
475
476 **Measurement of vascular permeability**
477 Pulmonary vascular permeability was measured by i.v. administration of Evans blue dye (0.2 ml 0.5% in
478 PBS) (50). One and half hours after Spike protein nasal administration, Evans blue dye was injected
479 intravenously. After another 1.5 hours the mice were perfused with PBS, and lungs and livers were
480 harvested, and dye extracted in formamide overnight at 55˚C. Dye concentrations were quantified by
481 measuring absorbance at 610 nm with subtraction of reference absorbance at 450 nm. The content of Evans
482 blue dye was determined by generating a standard curve from dye dilutions.
483
484 **NETosis assays**
485 Mouse bone marrow derived- or human neutrophils (> 97% purity) were resuspended in RPMI 1640 media
486 (1 x 10^6/ml) and incubated at 37°C in 5% CO_2 for 30 min. To induce NETosis, the cells were exposed to
487 N-formylmethionyl-leucyl-phenylalanine (fMLP, 1 µM); lipopolysaccharide (LPS, 10 ng/ml); tumor
488 necrosis factor-α (TNFα, 20 ng/ml); phorbol myristate acetate (PMA, 30 nM), or four different SARS-CoV
489 Spike protein preparations (0.1µg/ml or 1µg/ml) for 4 hours to overnight at 37°C. The cultures were
490 terminated by adding 4% PFA for 15 min. Helix NP™ NIR (0.1 µM; Biolegend) and DAPI (0.3 nM;
491 Biolegend) were added to detect NETs. Data acquisition (Helix NP™ NIR^+ $DAPI^+$ Cells) was done on
492 FACSCelesta SORP (BD) flow cytometer and analyzed with FlowJo software (Tree star). *In vitro* imaging
493 of NETosis was performed using a modified protocol from a previous report (51). The A549 cells were
494 plated 48 hr before imaging at 60% cell confluent. Fluorescently labeled SARS-CoV-2 Spike protein (Alexa
495 Fluor 488; 0.5 µg/ml) was added to the A549 cells 24 hr before human neutrophil seeding. Human
496 neutrophils were purified from whole blood by EasySep™ Direct Human Neutrophil Isolation Kit (Stem
497 cell). Purified human neutrophils were stained with Hoechst prior to seeding on SARS-CoV-2 Spike protein
498 pre-treated A549 cells in Propidium Iodide (PI, 1 µg/ml) containing culture media. Time-lapse images were
499 acquired with a Leica SP8 inverted 5 channels confocal microscope (Leica Microsystems) equipped with
500 40× oil objective, 0.95 NA (immersion medium used distilled water). The temperature of air (5% CO_2) was
501 maintained at 37.0± 0.5°C. Time interval between frames were set as 10 min for 5 hr acquisition. The loss
502 of nucleus of human neutrophils was detected by the loss of Hoechst signal and extracellular DNA released
503 by NETosis was labeled by PI signals.

504

505 **Fluorescent nanobead binding assay of SARS-CoV-2 Spike protein**

506 FluoSpheres™ NeutrAvidin™-Labeled Microspheres, 0.2 µm, yellow-green fluorescent (505/515), 1%
507 solids (Cat# F8774, Thermo Fisher Scientific Inc.) was used as a nanobead platform for SARS-CoV-2 Spike
508 protein conjugation. Fluorescent nanobead were directly counted and measured by BD FACSCelesta™
509 flow cytometer. A flow cytometer equipped with forward scatter (FSC) detector (Photodiode with 488/10
510 BP filter) and side scatter (SSC) detector (photomultiplier tube (PMT) with 488/10 BP filter) was tuned to
511 detect voltages up to 550 for FSC and 230 for SSC. Million counts of nanobeads were conjugated with 0.5
512 µg of SARS-CoV-2 Spike protein by interaction of Neutravidin on beads and Strep Tag II on recombinant
513 proteins. Nanobeads and SARS-CoV-2 Spike proteins in PBS were coupled at room temperature for one
514 hour and washed with 1 ml of PBS. Coupled nanobeads spun were down with benchtop centrifuge speed at
515 20,000 ×g, 4°C for 20 min. The nanobeads pellet was suspended with PBS concentration at 2×10^4/µl.
516 SARS-CoV-2 Spike protein couplings to nanobeads were tested with Alexa Fluor 647 conjugated SARS-
517 CoV-2 Spike neutralizing antibody (Cat# 40591-MM45, SinoBiological). To test binding ability of various
518 recombinant proteins (human ACE2, human Siglec-5, human Siglec-8, mouse ACE2, and mouse Siglec-F)
519 were directly conjugated with Alexa Fluor 647. SARS-CoV-2 Spike protein conjugated nanobeads (2×10^4
520 counts) in 20 µl of 1× HBSS (contains; 1 mM Ca^{2+}, 2 mM Mg^{2+}, 1 mM Mn^{2+} and 0.5% fatty acid free BSA)
521 buffer were incubated with 0.2 µg of fluorescent recombinant proteins at room temperature for 30 min.
522 Fluorescent antibody or recombinant protein biding on fluorescent nanobeads were directly counted and
523 measured by BD FACSCelesta™ flow cytometer.

524

525 **Thick section immunohistochemistry and confocal microscopy**

526 Immunohistochemistry was performed using a modified method of a previously published protocol (32,
527 52). Briefly, freshly isolated lungs were fixed in newly prepared 4% paraformaldehyde (Electron
528 Microscopy Science) overnight at 4 °C on an agitation stage. Fixed lungs were embedded in 4% low melting
529 agarose (Thermo Fisher Scientific) in PBS and sectioned with a vibratome (Leica VT-1000 S) at a 50 µm
530 thickness. Thick sections were blocked in PBS containing 10% fetal calf serum, 1 mg/ml anti-Fcγ receptor
531 (BD Biosciences), and 0.1% Triton X-100 (Sigma) for 30 min at room temperature. Sections were stained
532 overnight at 4°C on an agitation stage with Ly6G, Siglec-F, CD169, CD31, and F4/80, and labelled WGA.
533 Stained thick sections were microscopically analyzed using a Leica SP8 confocal microscope equipped
534 with an HC PL APO CS2 40× (NA, 1.30) oil objective (Leica Microsystem, Inc.) and images were
535 processed with Leica LAS AF software (Leica Microsystem, Inc.) and Imaris software v.9.9.1 64× (Oxford
536 Instruments plc). The intensities of fluorescent signals in regions of interests (ROI) were measured by LSA
537 AF Lite software (Leica Microsystem).

538

539 ***In vitro* imaging of HEK293 cells**

540 HEK293 cells were transfected using TransIT-293 transfection reagent (Mirus Bio LLC). For transient
541 expression of human Siglec-5-GFP 80% confluent HEK293 in 8 well chamber slide (0.25 ml/well) were
542 transfected by adding dropwise to each well 25 µl containing 0.25 µg of plasmid diluted in Opti-MEM with
543 a 1:4 (DNA/reagent) dilution of TransIT-293 Transfection Reagent. To generate a stable cell line of human
544 Siglec-5-GFP and human ACE2-OFP transfected HEK293 cells were sorted with FACS Aria II by GFP
545 and OFP signals. Sorted human Siglec-5-GFP transfected HEK293 cells were further selected with G418
546 (0.8 mg/ml) containing growth media and maintained with G418 (0.5 mg/ml) media. Sorted human ACE2-
547 OFP transfected HEK293 cells were further selected with hygromycin B (0.2 mg/ml) containing growth
548 media and maintained with hygromycin B (0.1 mg/ml) media. Transiently transfected HEK293 cells in 8
549 well chamber slide were directly imaged with a Leica SP8 inverted five channels confocal microscope
550 (Leica Microsystems). HEK293 cells, HEK293 Siglec-5-GFP, and HEK293 ACE2-OFP cell lines were
551 plated at a ratio of 1:1:1 (cell numbers) in 8 well chamber with normal media 18 hr prior to imaging.
552 Imaging was performed with a confocal microscope equipped with 40 × oil objective, 0.95 NA (immersion
553 medium used distilled water). The temperature of air (5% CO_2) was maintained at 37.0 ± 0.5°C. Fluorescent
554 SARS-CoV-2 Spike protein (Alexa Fluor 647) (1 µg/ml) was added into culture media. Images were
555 acquired with Leica LAS AF software (Leica Microsystem, Inc) and processed with Imaris software v.9.9.1
556 64× (Oxford Instruments plc).

557

558 **Time-lapse imaging of lung sections with confocal microscopy**

559 Lung slices were obtained from mouse lungs using a slightly modified published protocol (53). Briefly,
560 C57BL/6 mice were euthanized with overdose of Avertin (1 ml of 2.5% Avertin). The peritoneum was
561 opened, and the descending aorta cut allowing blood to pool in the abdomen. The trachea was cannulated,
562 and the lungs inflated with 37 °C 1.5% low-melting-point agarose (Cat# 50111, Lonza) prepared with RPMI
563 1640 media. Subsequently, the lungs were excised and rinsed with RPMI 1640 media. Isolated left lungs
564 were sectioned into six to eight 1-mm-thick transverse slices using a #10 scalpel blade. Lung slices were
565 placed in a pre-warmed cover glass chamber slide (Nalgene, Nunc) under a metal flat washer (M8- 5/16th
566 inches diameter). The chamber slide was then placed into the temperature control chamber on the
567 microscope. The temperature of air was monitored and maintained at 37.0± 0.5°C for 5% CO_2. Mounted
568 lung sections on the chamber slide were microscopically analyzed using a Leica SP8 confocal microscope
569 equipped with an HC PL APO CS2 40× (NA, 1.30) oil objective (Leica Microsystem, Inc.) and images
570 were processed with Leica LAS AF software (Leica Microsystem, Inc.). Lung slices were imaged a range

571 of depths (10-50 μm). Time-lapse images were processed with Imaris software v.9.9.1 64× (Oxford
572 Instruments plc).
573
574 **Intravital imaging**
575 The microanatomy of liver, spleen, heart, Peyer's patch, and inguinal LN were delineated by tail vein
576 injection of labelled antibodies before imaging. Antibodies used included CD31, blood vessels; F4/80,
577 Kupffer cells and macrophages; CD169, subcapsular macrophages; and Ly6G; neutrophils). The antibody
578 mixtures were injected 10 min before starting animal surgery. Fluorescently labelled spike proteins were
579 injected intravenously or at the mouse tail base as indicated. To image the liver or spleen a slightly modified
580 published protocol was used (54). Briefly, after initial anesthesia (Avertin 300 mg/kg, i.p.) the skin and
581 peritoneum were cut to expose the left lobe of the liver, or the left flank was cut below the costal margin to
582 expose the spleen. The visible organs were glued with n-butyl cyanoacrylate to a custom-made metal holder.
583 After attachment, the mouse was placed over a pre-warmed cover glass (Brain Research Laboratories)
584 window on universal mounting frame AK-Set (PECON®). The exposed organs were kept moist with saline
585 wetted gauze. The mounting frame was placed into the temperature control chamber on the microscope and
586 maintained at 37.0± 0.5°C. Once stabilized onto imaging stage/insert the mice received isoflurane (Baxter;
587 2% for induction of anesthesia, and 1 – 1.5% for maintenance, vaporized in an 80:20 mixture of oxygen
588 and air). For liver and spleen four-dimensional analysis of cell behavior, stacks of various numbers of
589 section (z step = 3, 5) were acquired every 5-30 sec to provide an imaging volume of 20 ~ 50 μm in depth.
590 Intact organ imaging of the heart, inguinal lymph node, or Peyer's patches was performed after mouse
591 sacrifice using same imaging procedure as used for liver/spleen imaging.
592 To image neutrophils in the cremaster muscle (31), mice received an intrascrotal injection of PBS,
593 BSA, IL-1β (50 ng in 300 μl saline, R&D Systems), Spike proteins, or IL-1b and Spike proteins. 90 min.
594 prior to imaging, the mice received injections of Avertin (300 mg/kg, i.p.) and fluorescently labeled
595 antibodies intravenously. Antibodies used directed against Gr-1, neutrophils; GPIbβ, platelets; and CD31,
596 blood vessel endothelium. The isolated cremaster tissue was exteriorized and stabilized onto the imaging
597 stage/insert with the tissue directly contacting the cover glass. The exposed tissue was kept moist with pre-
598 warmed saline (37°C). Once stabilized onto an imaging stage/insert the mouse received isoflurane (Baxter;
599 2% for induction of anesthesia, and 1 – 1.5% for maintenance, vaporized in an 80:20 mixture of oxygen
600 and air), and placed into a temperature-controlled chamber. Image stacks of optical sections (z step=1) were
601 routinely acquired at 20 – 30 sec intervals to provide an imaging volume of 15-25 μm. All imaging was
602 performed with a Leica SP8 inverted 5 channels confocal microscope (Leica Microsystems) equipped with
603 HC PL APO CS2 40× (NA, 1.30) oil objective. Sequences of image stacks were transformed into volume-

604 rendered four-dimensional videos using Imaris software v.9.9.1 64x (Oxford Instruments plc). Video
605 editing was performed using Adobe Premiere Pro 2022 (Adobe Systems Incorporated).
606
607 **Quantifications and Statistical Analyses**
608 All experiments were performed at least three times. Representative images were placed in figures. Primary
609 image data which was analyzed and calculated by Leica LAS AF software (Leica Microsystem, Inc.) or
610 Imaris software v.9.9.1 64× (Oxford Instruments plc). was acquired and processed with Microsoft Excel
611 software. Error bars with ±SEM, and p values were calculated with unpaired t-test in GraphPad Prism 9.3.1
612 (GraphPad software). $p<0.05$ was considered significantly different.
613
614
615 **REFERENCES**
616

617 1. Zhou P, Yang XL, Wang XG, Hu B, Zhang L, Zhang W, et al. A pneumonia outbreak associated
618 with a new coronavirus of probable bat origin. Nature. 2020;579(7798):270-3.
619 2. Wrapp D, Wang N, Corbett KS, Goldsmith JA, Hsieh CL, Abiona O, et al. Cryo-EM structure of
620 the 2019-nCoV spike in the prefusion conformation. Science. 2020;367(6483):1260-3.
621 3. Fan X, Cao D, Kong L, Zhang X. Cryo-EM analysis of the post-fusion structure of the SARS-CoV
622 spike glycoprotein. Nat Commun. 2020;11(1):3618.
623 4. Ke Z, Oton J, Qu K, Cortese M, Zila V, McKeane L, et al. Structures and distributions of SARS-
624 CoV-2 spike proteins on intact virions. Nature. 2020;588(7838):498-502.
625 5. Lan J, Ge J, Yu J, Shan S, Zhou H, Fan S, et al. Structure of the SARS-CoV-2 spike receptor-
626 binding domain bound to the ACE2 receptor. Nature. 2020;581(7807):215-20.
627 6. Benton DJ, Wrobel AG, Xu P, Roustan C, Martin SR, Rosenthal PB, et al. Receptor binding and
628 priming of the spike protein of SARS-CoV-2 for membrane fusion. Nature. 2020;588(7837):327-30.
629 7. Li F, Li W, Farzan M, Harrison SC. Structure of SARS coronavirus spike receptor-binding domain
630 complexed with receptor. Science. 2005;309(5742):1864-8.
631 8. Ou X, Liu Y, Lei X, Li P, Mi D, Ren L, et al. Characterization of spike glycoprotein of SARS-
632 CoV-2 on virus entry and its immune cross-reactivity with SARS-CoV. Nat Commun. 2020;11(1):1620.
633 9. Shang J, Wan Y, Luo C, Ye G, Geng Q, Auerbach A, et al. Cell entry mechanisms of SARS-CoV-
634 2. Proc Natl Acad Sci U S A. 2020;117(21):11727-34.
635 10. Shang J, Ye G, Shi K, Wan Y, Luo C, Aihara H, et al. Structural basis of receptor recognition by
636 SARS-CoV-2. Nature. 2020;581(7807):221-4.
637 11. Yan R, Zhang Y, Li Y, Xia L, Guo Y, Zhou Q. Structural basis for the recognition of SARS-CoV-
638 2 by full-length human ACE2. Science. 2020;367(6485):1444-8.
639 12. Lenza MP, Oyenarte I, Diercks T, Quintana JI, Gimeno A, Coelho H, et al. Structural
640 Characterization of N-Linked Glycans in the Receptor Binding Domain of the SARS-CoV-2 Spike Protein
641 and their Interactions with Human Lectins. Angew Chem Int Ed Engl. 2020;59(52):23763-71.
642 13. Walls AC, Tortorici MA, Frenz B, Snijder J, Li W, Rey FA, et al. Glycan shield and epitope
643 masking of a coronavirus spike protein observed by cryo-electron microscopy. Nat Struct Mol Biol.
644 2016;23(10):899-905.
645 14. Yang Q, Hughes TA, Kelkar A, Yu X, Cheng K, Park S, et al. Inhibition of SARS-CoV-2 viral
646 entry upon blocking N- and O-glycan elaboration. Elife. 2020;9.
647 15. Hoffmann M, Kleine-Weber H, Schroeder S, Kruger N, Herrler T, Erichsen S, et al. SARS-CoV-2
648 Cell Entry Depends on ACE2 and TMPRSS2 and Is Blocked by a Clinically Proven Protease Inhibitor.
649 Cell. 2020;181(2):271-80 e8.

650 16. Hoffmann M, Kleine-Weber H, Pohlmann S. A Multibasic Cleavage Site in the Spike Protein of
651 SARS-CoV-2 Is Essential for Infection of Human Lung Cells. Mol Cell. 2020;78(4):779-84 e5.
652 17. Takeda M. Proteolytic activation of SARS-CoV-2 spike protein. Microbiol Immunol.
653 2022;66(1):15-23.
654 18. Errico JM, Adams LJ, Fremont DH. Antibody-mediated immunity to SARS-CoV-2 spike. Adv
655 Immunol. 2022;154:1-69.
656 19. Troyer Z, Alhusaini N, Tabler CO, Sweet T, de Carvalho KIL, Schlatzer DM, et al. Extracellular
657 vesicles carry SARS-CoV-2 spike protein and serve as decoys for neutralizing antibodies. J Extracell
658 Vesicles. 2021;10(8):e12112.
659 20. Swank Z, Senussi Y, Manickas-Hill Z, Yu XG, Li JZ, Alter G, et al. Persistent circulating SARS-
660 CoV-2 spike is associated with post-acute COVID-19 sequelae. Clin Infect Dis. 2022.
661 21. Theoharides TC. Could SARS-CoV-2 Spike Protein Be Responsible for Long-COVID Syndrome?
662 Mol Neurobiol. 2022;59(3):1850-61.
663 22. Thanh Le T, Andreadakis Z, Kumar A, Gomez Roman R, Tollefsen S, Saville M, et al. The COVID-
664 19 vaccine development landscape. Nat Rev Drug Discov. 2020;19(5):305-6.
665 23. Lamprinou M, Sachinidis A, Stamoula E, Vavilis T, Papazisis G. COVID-19 vaccines adverse
666 events: potential molecular mechanisms. Immunol Res. 2023:1-17.
667 24. Hsieh CL, Goldsmith JA, Schaub JM, DiVenere AM, Kuo HC, Javanmardi K, et al. Structure-
668 based design of prefusion-stabilized SARS-CoV-2 spikes. Science. 2020;369(6510):1501-5.
669 25. Yurkovetskiy L, Wang X, Pascal KE, Tomkins-Tinch C, Nyalile TP, Wang Y, et al. Structural and
670 Functional Analysis of the D614G SARS-CoV-2 Spike Protein Variant. Cell. 2020;183(3):739-51 e8.
671 26. Zhang L, Jackson CB, Mou H, Ojha A, Peng H, Quinlan BD, et al. SARS-CoV-2 spike-protein
672 D614G mutation increases virion spike density and infectivity. Nat Commun. 2020;11(1):6013.
673 27. Volz E, Hill V, McCrone JT, Price A, Jorgensen D, O'Toole A, et al. Evaluating the Effects of
674 SARS-CoV-2 Spike Mutation D614G on Transmissibility and Pathogenicity. Cell. 2021;184(1):64-75 e11.
675 28. Aida Y, Pabst MJ. Removal of endotoxin from protein solutions by phase separation using Triton
676 X-114. J Immunol Methods. 1990;132(2):191-5.
677 29. Hetzel M, Ackermann M, Lachmann N. Beyond "Big Eaters": The Versatile Role of Alveolar
678 Macrophages in Health and Disease. Int J Mol Sci. 2021;22(7).
679 30. Matthew CB, Sils IV, Bastille AM. Tissue-specific extravasation of albumin-bound Evans blue in
680 hypothermic and rewarmed rats. Can J Physiol Pharmacol. 2002;80(3):233-43.
681 31. Yan SL, Hwang IY, Kamenyeva O, Kabat J, Kim JS, Park C, et al. Unrestrained Galpha(i2)
682 Signaling Disrupts Neutrophil Trafficking, Aging, and Clearance. Front Immunol. 2021;12:679856.
683 32. Park C, Arthos J, Cicala C, Kehrl JH. The HIV-1 envelope protein gp120 is captured and displayed
684 for B cell recognition by SIGN-R1(+) lymph node macrophages. Elife. 2015;4.
685 33. Youn YJ, Lee YB, Kim SH, Jin HK, Bae JS, Hong CW. Nucleocapsid and Spike Proteins of SARS-
686 CoV-2 Drive Neutrophil Extracellular Trap Formation. Immune Netw. 2021;21(2):e16.
687 34. Perez-Zsolt D, Erkizia I, Pino M, Garcia-Gallo M, Martin MT, Benet S, et al. Anti-Siglec-1
688 antibodies block Ebola viral uptake and decrease cytoplasmic viral entry. Nat Microbiol. 2019;4(9):1558-
689 70.
690 35. Perez-Zsolt D, Munoz-Basagoiti J, Rodon J, Elosua-Bayes M, Raich-Regue D, Risco C, et al.
691 SARS-CoV-2 interaction with Siglec-1 mediates trans-infection by dendritic cells. Cell Mol Immunol.
692 2021;18(12):2676-8.
693 36. Hammonds JE, Beeman N, Ding L, Takushi S, Francis AC, Wang JJ, et al. Siglec-1 initiates
694 formation of the virus-containing compartment and enhances macrophage-to-T cell transmission of HIV-
695 1. PLoS Pathog. 2017;13(1):e1006181.
696 37. Connolly NP, Jones M, Watt SM. Human Siglec-5: tissue distribution, novel isoforms and domain
697 specificities for sialic acid-dependent ligand interactions. Br J Haematol. 2002;119(1):221-38.
698 38. Sefik E, Qu R, Junqueira C, Kaffe E, Mirza H, Zhao J, et al. Inflammasome activation in infected
699 macrophages drives COVID-19 pathology. Nature. 2022;606(7914):585-93.

39. Vora SM, Lieberman J, Wu H. Inflammasome activation at the crux of severe COVID-19. Nat Rev Immunol. 2021;21(11):694-703.
40. Aizawa H, Zimmermann N, Carrigan PE, Lee JJ, Rothenberg ME, Bochner BS. Molecular analysis of human Siglec-8 orthologs relevant to mouse eosinophils: identification of mouse orthologs of Siglec-5 (mSiglec-F) and Siglec-10 (mSiglec-G). Genomics. 2003;82(5):521-30.
41. Tsai CM, Riestra AM, Ali SR, Fong JJ, Liu JZ, Hughes G, et al. Siglec-14 Enhances NLRP3-Inflammasome Activation in Macrophages. J Innate Immun. 2020;12(4):333-43.
42. Honzke K, Obermayer B, Mache C, Fathykova D, Kessler M, Dokel S, et al. Human lungs show limited permissiveness for SARS-CoV-2 due to scarce ACE2 levels but virus-induced expansion of inflammatory macrophages. Eur Respir J. 2022;60(6).
43. Lu Q, Liu J, Zhao S, Gomez Castro MF, Laurent-Rolle M, Dong J, et al. SARS-CoV-2 exacerbates proinflammatory responses in myeloid cells through C-type lectin receptors and Tweety family member 2. Immunity. 2021;54(6):1304-19 e9.
44. Sun W, Wu W, Jiang N, Ge X, Zhang Y, Han J, et al. Highly Pathogenic PRRSV-Infected Alveolar Macrophages Impair the Function of Pulmonary Microvascular Endothelial Cells. Viruses. 2022;14(3).
45. Bernard I, Limonta D, Mahal LK, Hobman TC. Endothelium Infection and Dysregulation by SARS-CoV-2: Evidence and Caveats in COVID-19. Viruses. 2020;13(1).
46. Nader D, Kerrigan SW. Molecular Cross-Talk between Integrins and Cadherins Leads to a Loss of Vascular Barrier Integrity during SARS-CoV-2 Infection. Viruses. 2022;14(5).
47. Dominguez-Soto A, Aragoneses-Fenoll L, Gomez-Aguado F, Corcuera MT, Claria J, Garcia-Monzon C, et al. The pathogen receptor liver and lymph node sinusoidal endotelial cell C-type lectin is expressed in human Kupffer cells and regulated by PU.1. Hepatology. 2009;49(1):287-96.
48. Kondo Y, Larabee JL, Gao L, Shi H, Shao B, Hoover CM, et al. L-SIGN is a receptor on liver sinusoidal endothelial cells for SARS-CoV-2 virus. JCI Insight. 2021;6(14).
49. Sung PS, Yang SP, Peng YC, Sun CP, Tao MH, Hsieh SL. CLEC5A and TLR2 are critical in SARS-CoV-2-induced NET formation and lung inflammation. J Biomed Sci. 2022;29(1):52.
50. Zhou Y, Schneider DJ, Morschl E, Song L, Pedroza M, Karmouty-Quintana H, et al. Distinct roles for the A2B adenosine receptor in acute and chronic stages of bleomycin-induced lung injury. J Immunol. 2011;186(2):1097-106.
51. Hoppenbrouwers T, Autar ASA, Sultan AR, Abraham TE, van Cappellen WA, Houtsmuller AB, et al. In vitro induction of NETosis: Comprehensive live imaging comparison and systematic review. PLoS One. 2017;12(5):e0176472.
52. Park C, Hwang IY, Kehrl JH. The Use of Intravital Two-Photon and Thick Section Confocal Imaging to Analyze B Lymphocyte Trafficking in Lymph Nodes and Spleen. Methods Mol Biol. 2018;1707:193-205.
53. Pieretti AC, Ahmed AM, Roberts JD, Jr., Kelleher CM. A novel in vitro model to study alveologenesis. Am J Respir Cell Mol Biol. 2014;50(2):459-69.
54. Matsumoto S, Kikuta J, Ishii M. Intravital Imaging of Liver Cell Dynamics. Methods Mol Biol. 2018;1763:137-43.

Acknowledgements: The authors thank Dr. Anthony Fauci for long standing encouragement**.**

Funding: This work was supported by Intramural Research Program of National Institute of Allergy and Infectious Diseases.

Author Contribution: CP performed most of the mouse work; IYH performed the flow cytometry and macrophage cytokine production; SLY performed the cremaster imaging, SV, DW, and DVR purified the

recombinant proteins, CC and JA supervised the protein purification and provided helpful advice, JHK wrote the manuscript and oversaw the project.

Competing interests: The authors declare they have no competing interests. The content is solely the responsibility of the authors and does not necessarily represent the official views of the National Institutes of Health

Data and Material Availability: The primary imaging files are available from the corresponding author.

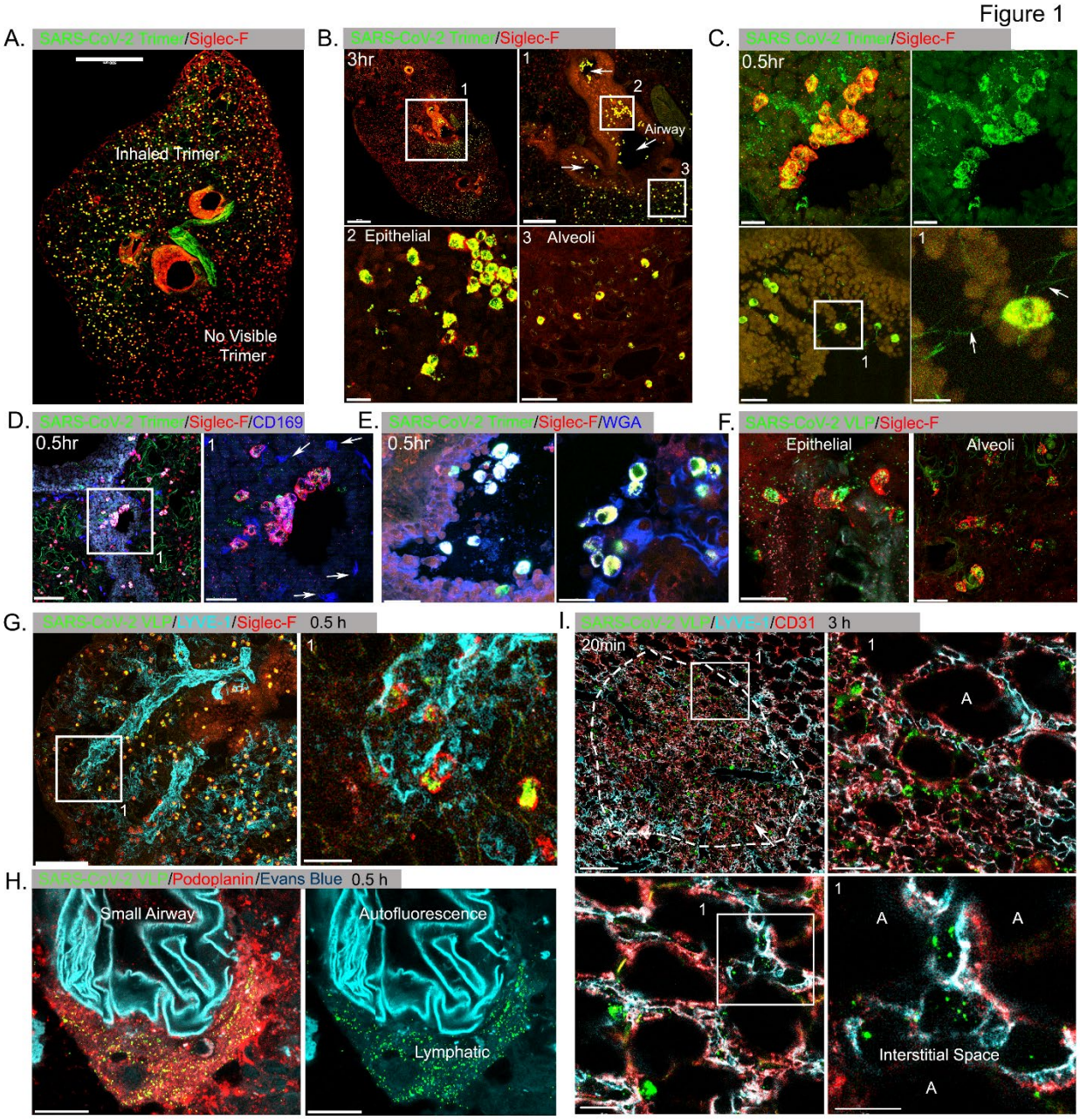

754

755 **Figure 1.** Lung images following intranasal administered SARS-CoV-2 Spike protein. **(A)** Confocal
756 micrograph of a lung section 18 hr post SARS-CoV-2 Spike protein (Trimer) inhalation. Alveolar
757 macrophages (AMs) visualized with Siglec-F antibody. Alexa Fluor 488 conjugated recombinant SARS-
758 CoV-2 Spike protein (3 µg in 50 µl of saline) was inoculated by nasal inhalation. Spike-reached lung region
759 (Inhaled Trimer) and non-reached area (No visible Trimer) noted on the micrograph. Scale bar, 500 µm.
760 **(B)** Confocal micrographs of lung collected at 3 hr post Spike protein inhalation. AMs in the large airway
761 and alveoli (upper left) area is shown. ROI-1 (box1) (upper right) is enlarged, and arrows indicate large

762 airways. ROI-2 (Box 2) (lower left) shows AMs bearing SARS-CoV-2 Spike protein on airway epithelial
763 cells. ROI-3 (Box 3) (lower left) shows Spike protein bearing AMs in alveoli. Scale bars, 500, 200, 20, and
764 50 µm. (**C**) Confocal micrographs of lung collected at 0.5 hr post SARS-CoV-2 Spike protein inhalation.
765 AMs were visualized with Siglec-F antibody (upper left & right). AMs connected to each other (lower left)
766 via tunneling nanotubes (arrows) (lower right). Scale bars, 20, 20, 30, and 10 µm. **(D & E)** Confocal
767 micrographs of lung collected at 0.5 hr post Spike inhalation. SARS-CoV-2 Spike protein (green) on airway
768 epithelium and CD169^{+} macrophages (D). Arrows indicate CD169^{+} macrophages (right). Scale bars, 100
769 and 30 µm. AMs with SARS-CoV-2 Spike protein and Mucin (Alexa Fluor 647 conjugated wheat germ
770 agglutin, WGA) on airway epithelium (E). Scale bars, 30 and 20 µm. **(F)** Confocal micrographs of lung
771 collected at 2 hr post SARS-CoV-2 Spike protein incorporated VLP inhalation (green). AMs (red, Siglec-
772 F) on epithelium (left) and in alveoli (right). Scale bars, 20 µm. **(G)** Confocal micrographs of lung collected
773 at 0.5 hr post SARS-CoV-2 Spike VLP (green) inhalation. AMs (red, Siglec-F antibody) and lung
774 vasculatures visualized LYVE-1 (cyan) (top, left). LYVE-1^{+} vasculature associated AMs bearing VLPs is
775 highlighted (box) and enlarged (top, right). Scale bars, 100 and 25 µm. **(H)** A confocal micrograph shows
776 a lung lymphatic vasculature visualized with Podoplanin antibody. Fifty microliters of a mixture of Evans
777 blue (cyan) (5 µg) and Spike bearing VLPs (green) (0.5 million counts) were applied to the mouse nose.
778 VLPs in lymphatics associated with a small airway highlighted (right). Scale bars, 20 µm. **(I)** Confocal
779 micrographs of lung collected 20 min post Spike incorporated VLP (green) inhalation. Lung vasculatures
780 visualized CD31 (red) and LYVE-1 (cyan). Damaged lung tissue is indicated (dotted line) (upper left).
781 Border of damaged tissue and intact alveoli (box) is enlarged (upper right). A lymphatic structure was
782 stained by LYVE-1 in intact alveolus is highlighted (lower left). An image of VLPs in LYVE-1^{+} lymphatic
783 portal in alveoli (box) is enlarged (lower right). "A" indicates alveolus. Scale bars, 100, 20, 25, and 10 µm.
784
785
786
787
788
789
790

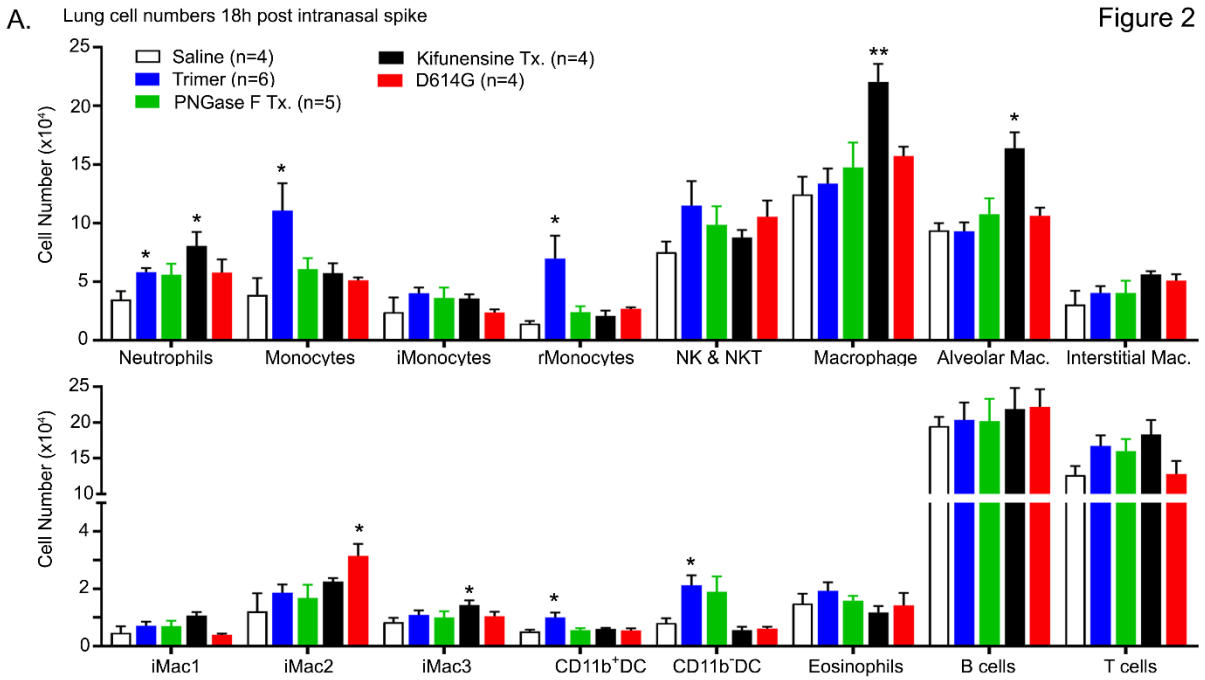

B. Lung cell uptake at 18h post intranasal spike

Cell Type	Background	Trimer (n=6)	PNGase F Tx. (n=5)	Kifunensine Tx. (n=8)	D614G (n=4)
		Percentage			
Neutrophils	1.245 ± 0.149	3.395 ± 0.916	2.604 ± 0.998	2.084 ± 0.421	4.645 ± 1.484
rMono	1.130 ± 0.450	2.888 ± 0.759	1.204 ± 0.419	0.684 ± 0.095	6.983 ± 1.168 **
iMono	1.033 ± 0.159	3.565 ± 0.805	1.92 ± 0.701	0.856 ± 0.175 *	4.700 ± 0.669
AMac	1.025 ± 0.376	77.467 ± 5.924	62.906 ± 16.825 **	39.025 ± 5.412 ****	84.325 ± 1.674
iMac1	2.980 ± 0.720	9.288 ± 3.234	3.102 ± 1.242	2.754 ± 0.368	9.533 ± 1.162
iMac2	1.408 ± 0.098	13.583 ± 3.234	5.386 ± 1.250 *	2.093 ± 0.187 ***	8.870 ± 1.811
iMac3	1.755 ± 0.769	31.800 ± 7.223	36.642 ± 13.330	18.403 ± 5.740****	10.420 ± 2.022****
Eosinophils	1.438 ± 0.092	2.008 ± 0.539	1.758 ± 0.344	1.736 ± 0.272	5.125 ± 0.428 *
CD11b+DC	2.225 ± 0.597	5.962 ± 1.136	4.898 ± 1.004	7.383 ± 2.163	9.275 ± 1.126 *
CD11b-DC	2.240 ± 0.251	3.702 ± 0.633	5.372 ± 1.056	3.644 ± 0.477	7.143 ± 1.422 *
NK&NKT	0.658 ± 0.244	1.110 ± 0.176	1.014 ± 0.363	0.469 ± 0.100	3.688 ± 0.526
B	0.328 ± 0.099	1.055 ± 0.196	0.906 ± 0.293	0.386 ± 0.099	2.160 ± 0.264
T	0.156 ± 0.068	1.015 ± 0.360	0.432 ± 0.149	0.200 ± 0.027	2.338 ± 0.468

Figure 2. Lung leukocyte profile following intranasal administration of SARS-CoV-2 Spike proteins. **(A)** Leukocyte numbers in isolated lung tissue. Eighteen hr post intranasal administration of indicated Spike proteins lung tissue collected, processed, and leukocyte cell numbers determined by flow cytometry. Numbers of mice analyzed are indicated. Data mean +/- SEM, *$p < 0.05$; **$p < 0.005$. **(B)** SARS-CoV-2 Spike protein uptake by lung leukocytes 18 hr following intranasal inoculation. Flow cytometry results from indicated mice. Values significantly different from the WT SARS-CoV-2 protein (Trimer) are indicated, *$p < 0.05$; **$p < 0.01$; ***$p < 0.005$. ****$p<0.001$.

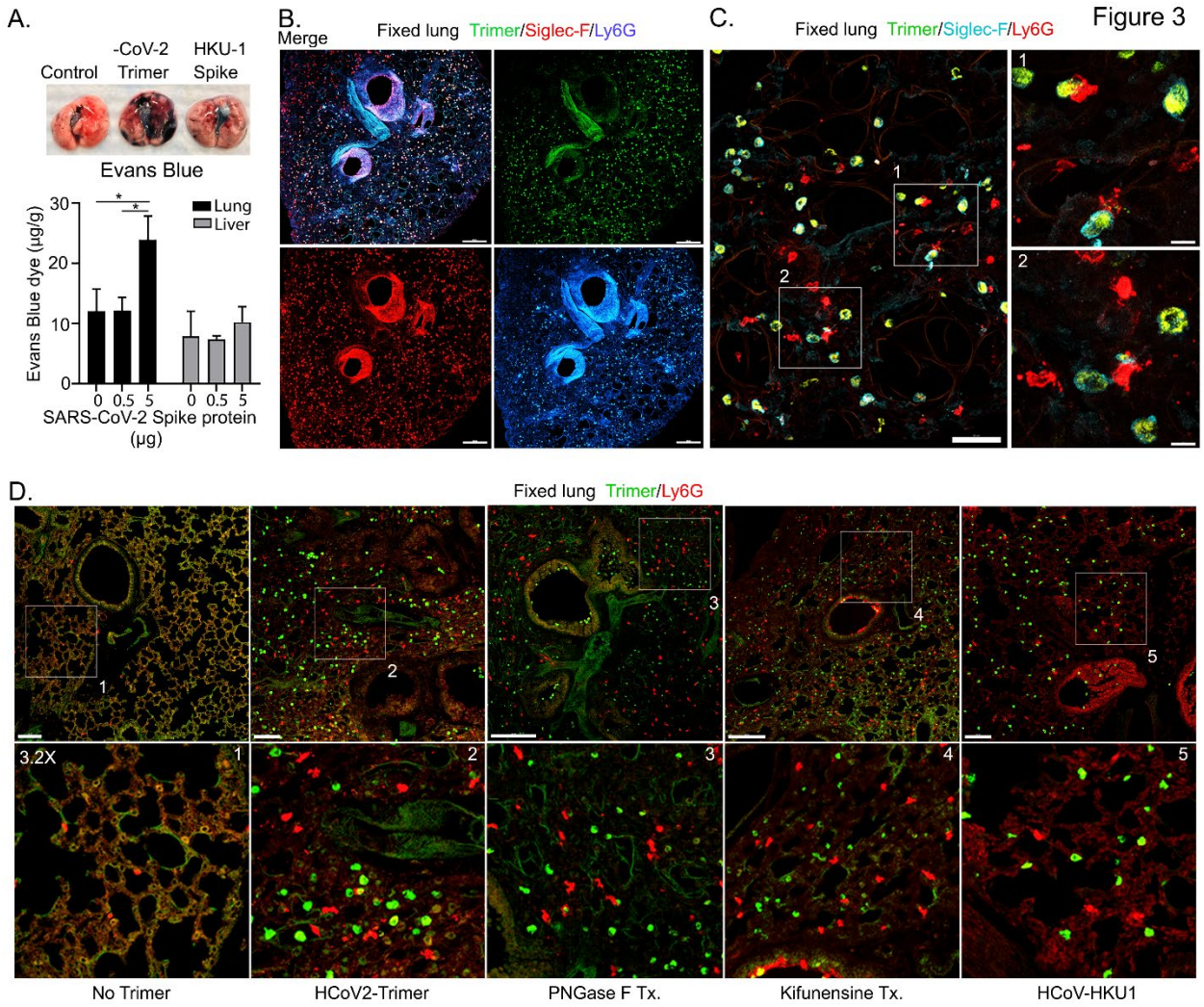

Figure 3. Increased lung vascular permeability and neutrophil localization following intranasal SARS-CoV-2 Spike protein. **(A)** Tissue photographs of lungs collected 2.5 hr post Spike protein (Trimer) inhalation. Evans blue (200 ul of 5 mg/ml, PBS) was injected i.v. 1.5 hr post intranasal Spike administration. Lungs collected 1 hr after Evans blue injection. Evans blue amounts in lung and liver tissue are shown. **(B)** Confocal micrographs of lung collected at 18 hr post Spike protein. AMs and neutrophils detected with Siglec-F and Ly-6G antibodies, respectively. Scale bar, 500 µm. **(C)** Confocal micrographs of lung collected at 3 hr post SARS-CoV-2 Spike protein inhalation show SARS-CoV-2 Spike protein (green), neutrophils (red), and AMs (cyan). ROI-1 and -2 (boxes), show contact between AMs and neutrophils and are enlarged in the right panels. Scale bars, 50 and 10 µm. **(D)** Confocal micrographs of lung collected at 3 hr post each SARS-CoV-2 Spike proteins inhalation show SARS-CoV-2 Spike protein (green) and neutrophils (red). From left to right of panels show saline (No Trimer), SARS-CoV-2 Spike protein (HCoV2-Trimer), PNGase F treated SARS-CoV-2 Spike protein (PNGase F Tx.), SARS-CoV-2 Spike protein purified from Kifunensine treated cells (Kifunensine Tx.), and human coronavirus HKU1

813 (HCoV-HKU1) Spike Protein. ROIs in each upper panel (boxes) are enlarged (3.2× magnification) in lower
814 panels. Scale bars, 200 µm. *p < 0.05.
815

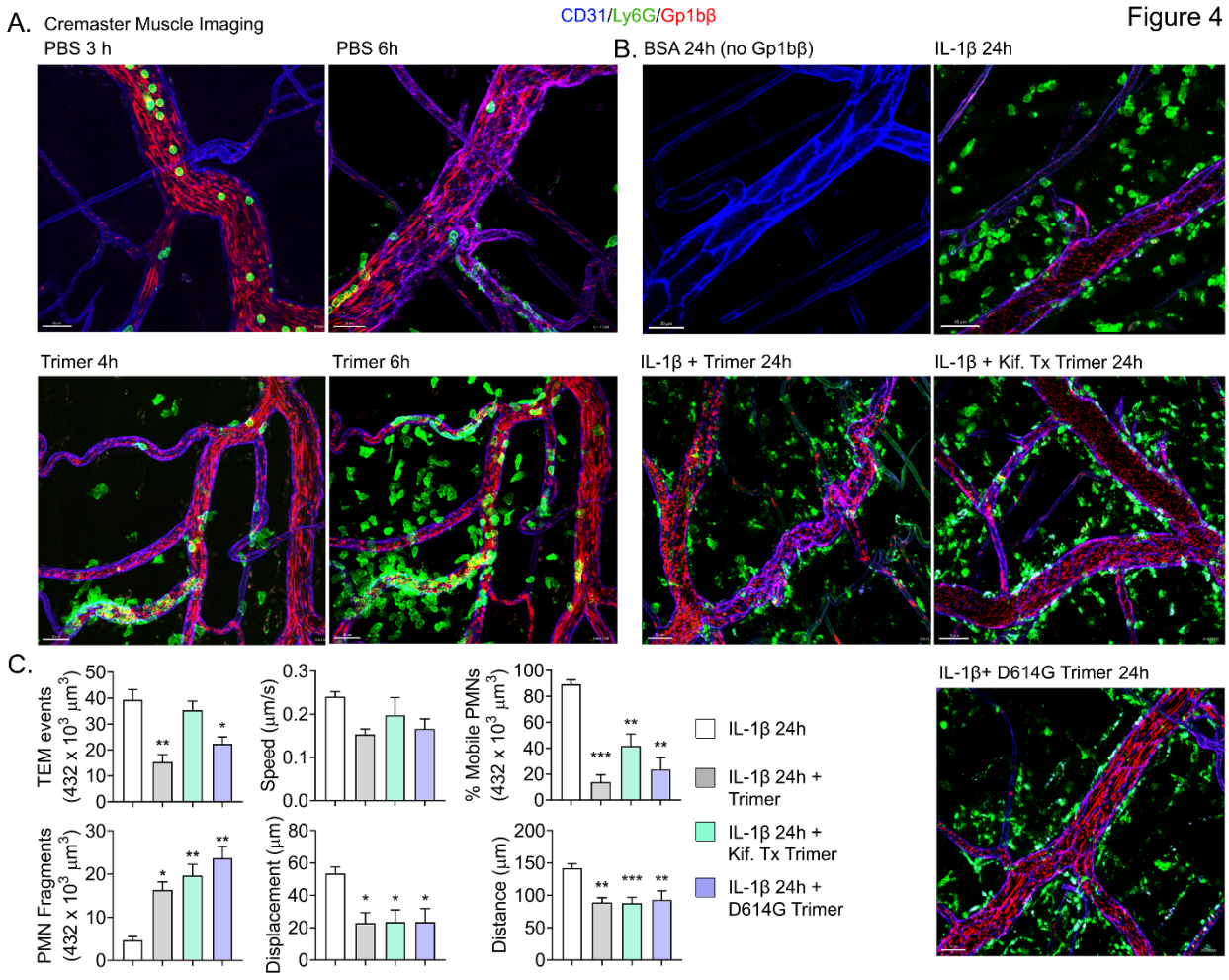

816
817 **Figure 4.** Mouse neutrophil damage following intrascrotal injections of Spike proteins. **(A & B)** Confocal
818 snapshots of time-lapse movie of blood vessels in the cremaster muscle following PBS, BSA, Spike protein
819 preparations (Trimer), IL-1β, or IL-1β plus Spike protein (5 µg) at indicated time points. Fluorescently
820 labelled CD31, Ly6G, and Gp1bβ outlined the blood vessel endothelium, neutrophils, and platelets,
821 respectively. Scale bars, 30 µm, except far right top and middle panels, 40 µm **(C)** Analysis of imaging
822 data. The number of transendothelial migration (TEM) events recorded, neutrophil (PMN) fragments, and
823 % mobile neutrophils in a defined imaging space over 20 min. Results of neutrophil tracking in the same
824 defined volume including speed, displacement, and distance. Imaris software used for the tracking. *p <
825 0.05; **p < 0.005.
826

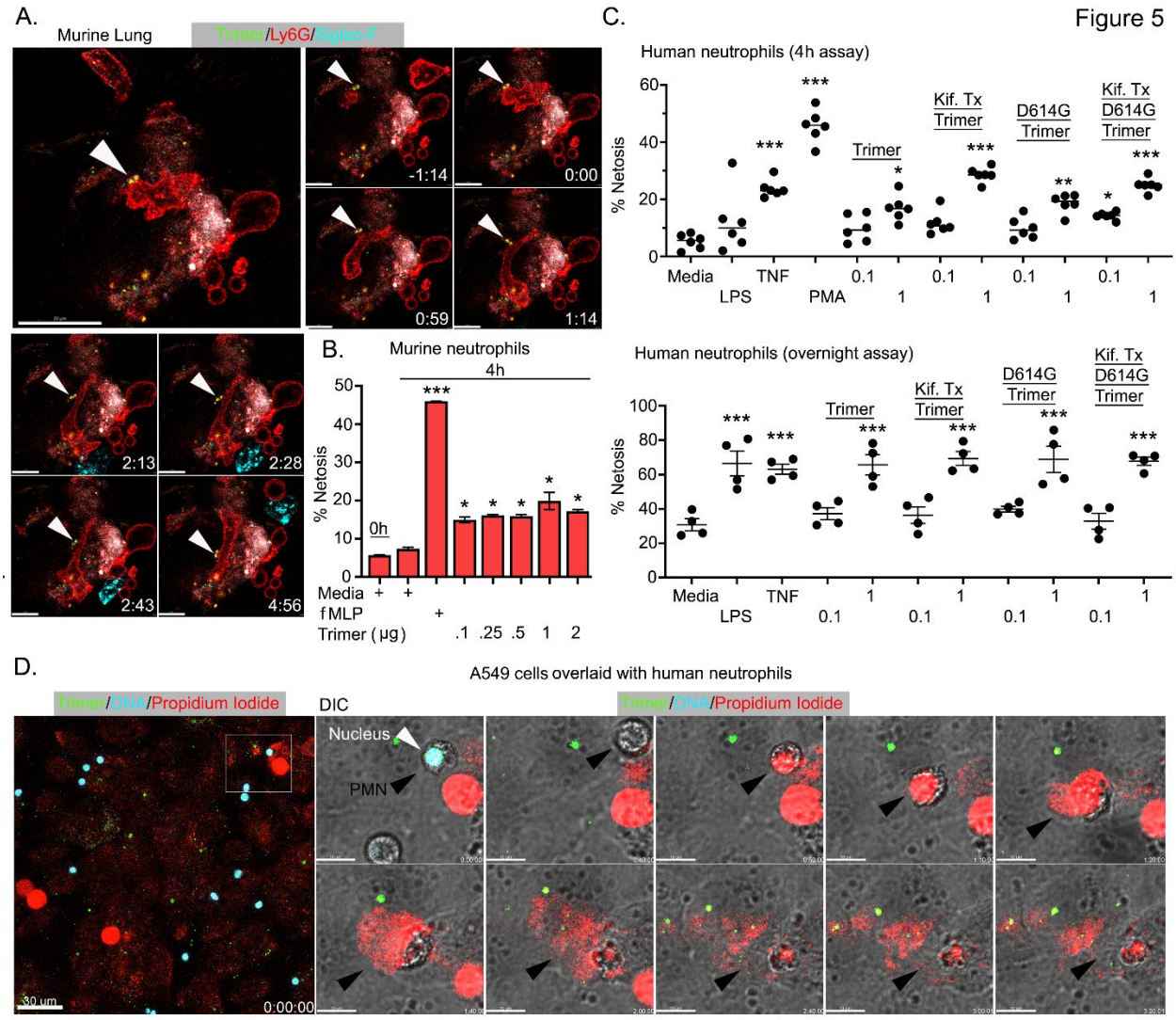

Figure 5. Neutrophil injury following exposure to SARS-CoV-2 Spike proteins. **(A)** Time-lapse images of a freshly sliced lung section 3 hr after SARS-CoV-2 Spike protein inhalation. Neutrophils (Ly6G) and AMs (Siglec-F) were visualized by injected fluorescently tagged antibodies. Serial images show neutrophil behavior on Spike protein (Trimer) bearing cells. Arrowheads indicate Spike protein deposition. The time banner is set to 0:00 as neutrophil contacts Spike protein. Scale bars, 100, 25, and 20 µm. **(B)** Purified murine bone marrow neutrophils were exposed to increasing concentrations of Spike protein or fMLP (N-formyl-methionyl-leucyl-phenylalanine for 4 hours or not. The percentage of neutrophils undergoing NETosis was measured by flow cytometry. **(C)** Purified human peripheral blood neutrophils were exposed to various Spike protein preparations, lipopolysaccharide (LPS), tumor necrosis factor-α (TNF) or phorbol myristate acetate (PMA). Graphs show the percentage of DAPI^{+}Helix NP NIR^{+} cells after either 4 hr or overnight culture. Each point represents a different donor. **(D)** A still image of *in vitro* time-lapse movie shows exposed neutrophil DNA (red, propidium iodide), neutrophil nucleus (cyan, Hoechst), and SARS-

CoV-2 Spike protein (trimer, green) bearing A549 cells. Plated A549 cells were treated with Spike protein (0.5 µg/ml) 24 hr prior to Hoechst-stained human neutrophil seeding. Propidium iodide (1 µg/ml) was added to the culture media and time-lapse images acquired every 10 min for 5 hr. Sequential DIC images overlay with fluorescent images show neutrophil NETosis. White arrowhead indicates a neutrophil's intact nucleus (cyan, Hoechst). Black arrowheads delineate a neutrophil undergoing NETosis as detected by exposed DNA (red). Scale bars, 30 and 10 µm. *p < 0.05; **p < 0.01; ***p < 0.005.

Figure 6

A.

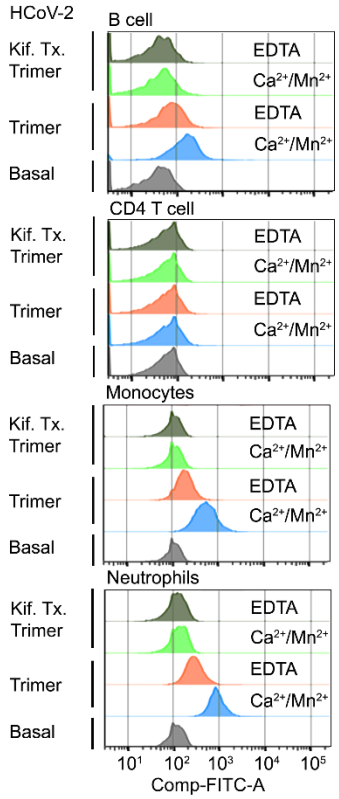

B.

Cell Type	Buffer	HKU-1 S1 (n=2)	HCoV-2 S1 (n=2)	HCoV-2 Trimer (n=8)	Kif. Tx. Trimer (n=2)
B cells	Mn^{2+}/Ca^{2+}	1.000 ±0.150	23.390 ±9.210	54.955 ±9.235	14.225 ±5.775
	EDTA	0.585 ± 0.055	11.565 ±9.135	21.099 ±7.029	1.995 ±0.675
CD4 T cells	Mn^{2+}/Ca^{2+}	0.165 ±0.025	2.410 ±2.010	1.656 ±0.222	0.635 ±0.486
	EDTA	0.190 ±0.060	1.995 ±1.545	0.761 ±0.216	0.180 ±0.060
CD8 T cells	Mn^{2+}/Ca^{2+}	0.380 ±0.010	5.785 ±4.315	8.824 ±2.483	1.380 ±0.940
	EDTA	0.355 ±0.025	5.130 ±3.330	2.479 ±0.595	0.225 ±0.095
NKT cells	Mn^{2+}/Ca^{2+}	4.890 ±0.540	9.095 ±4.105	15.355 ±2.865	10.750 ±6.450
	EDTA	3.210 ±1.180	6.455 ±3.325	6.455 ±3.325	2.300 ±2.010
NK	Mn^{2+}/Ca^{2+}	0.210 ±0.080	26.350 ±1.560	5.018 ±1.665	0.650 ±0.470
	EDTA	0.805 ±0.225	1.405 ±1.195	0.394 ±0.114	0.022 ±0.022
Neutrophils	Mn^{2+}/Ca^{2+}	1.215 ±0.265	23.030 ±8.470	72.500 ±10.880	5.420 ± 1.420
	EDTA	0.600 ±0.270	7.695 ±4.705	27.126 ±6.769	0.435 ± 0.235
Classical Monocytes	Mn^{2+}/Ca^{2+}	2.755 ±0.615	71.200 ±25.900	86.913 ±6.872	6.885 ± 3.215
	EDTA	2.075 ±1.325	43.100 ±25.800	46.394 ±11.433	1.461 ±1.410
Activated Monocytes	Mn^{2+}/Ca^{2+}	6.055 ±1.925	71.050 ±25.750	68.300 ±14.378	6.735 ± 4.065
	EDTA	2.120 ±0.100	44.600 ±27.300	31.766 ±12.407	1.550 ± 0.620
Myeloid Dendritic Cells (mDC)	Mn^{2+}/Ca^{2+}	1.385 ±1.215	30.850 ±20.350	43.800 ±10.643	6.180 ± 3.360
	EDTA	0.805 ±0.225	11.620 ±9.880	13.504 ±5.444	1.710 ± 0.840
Plasmacytoid Dendritic Cells (pDC)	Mn^{2+}/Ca^{2+}	2.885 ±2.885	38.255 ±27.645	33.239 ±10.560	20.050 ± 20.050
	EDTA	1.370 ±1.370	4.515 ±0.515	2.225 ±0.625	0.000 ± 0.000

Figure 6. Binding of recombinant SARS-CoV Spike proteins to human peripheral blood leukocytes **(A)** Representative flow cytometry histograms of various cell populations prepared from whole blood incubated with labeled recombinant SARS-CoV-2 Spike protein (Trimer), or Spike protein from Kifunensine treated cell (Kif. Tx. Trimer), binding done in the presence of Ca^{2+}/Mn^{2+} or EDTA. **(B)** Percentage of various cell populations prepared from whole blood that bound labelled HKU1 S1 protein (HKU-1 S1), SARS-CoV-2 S1 protein (HCoV-2 S1), SARS-CoV-2 Spike protein (HCoV-2 Trimer), or Spike protein purified from Kifunesine treated cells (Kif. Tx. Trimer). Binding done in the presence of Ca^{2+}/Mn^{2+} or EDTA and assessed by flow cytometry. Data are from two-eight independent experiments. Highest binding (mean fluorescent intensity) for each cell type designated with red outline.

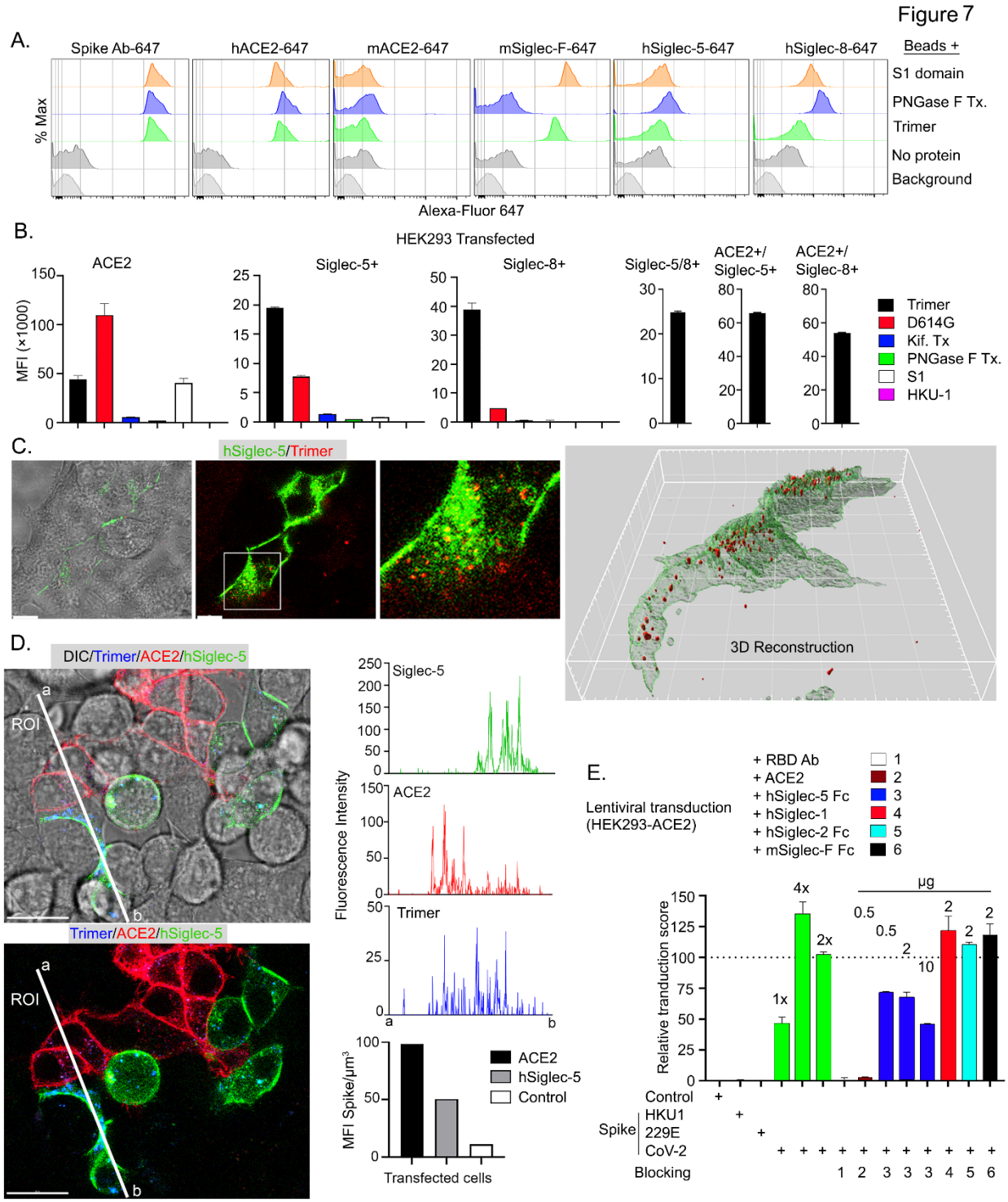

Figure 7. Role of Siglecs in SARS-CoV-2 Spike capture. **(A)** Histograms show mean fluorescence of conjugated recombinant proteins and antibody on nanobeads that are coated with indicated SARS-CoV-2 Spike proteins. Background signal (weak gray) measured with uncoated beads. No protein (gray) means that uncoated beads were incubated with indicated labelled recombinant protein or antibody. **(B)** Flow cytometry assessment of indicated Spike proteins binding to HEK293 cell permanently transfected with ACE2, various Siglecs, or a combination. Dual

transfected HEK293 cells noted as Siglec-5/8+, ACE2/Siglec-5+, and ACE2/Siglec-8+. Labelled recombinant proteins were incubated with 5×10^3 HEK293 cells on ice for 30 min. Data shown as mean fluorescent intensity. **(C)** DIC and confocal micrographs showing SARS-CoV-2 Spike (Trimer, red) protein acquisition by human Siglec-5-GFP transfected HEK293. ROI-1 in the middle panel is enlarged at the right panel. A 3D-reconstituted volume image of Siglec-5 transfected cell (far right), shows Siglec-5 mediated Spike protein acquisition. Scale bars, 30 and 10 μm. **(D)** DIC and confocal images show SARS-CoV-2 Spike protein acquisition by human Siglec-5-GFP or ACE2-OFP transfected HEK293. Equal numbers of stable-transfectants expressing Siglec-5-GFP or ACE2-OFP, and non-transfectant were seeded together. Spike protein (Trimer, blue) was added 1 hr prior to imaging. In a region of interest (ROI) line a-b fluorescence intensity of Siglec-5-GFP, ACE2-OFP and SARS-CoV-2 spike trimer were analyzed. Fluorescent intensity graphs show fluorescence intensity of each signal in ROI. Amount of 3D-reconstructed volume of SARS-CoV-2 spike protein in each stable cell and HEK293 cell were analyzed and plotted in graph. Graphs shows quantity of mean fluorescence intensity of SARS-CoV-2 spike protein in unit volume (μm^3) of indicated cell types. Scale bars, 20 μm. **(E)** Transduction of Spike protein expressing lentiviruses into ACE2/HEK293 transfectants. Lentiviruses envelop proteins: control (none), human coronavirus HKU-1 Spike protein (HKU1), human coronavirus 229E Spike protein (229E), and SARS-CoV-2 Spike protein (CoV-2) are indicated. The volume of virus concentrates used for transduction is denoted as 1×, 2×, and 4× on the graph (bright green bars). Transduction scores were normalized to 2× transduction efficiency. Various recombinant proteins or antibody used for inhibition assay are indicated. Recombinant proteins or RBD neutralizing antibody were added 0.5 hr before lentivirus transduction. 3 days later GFP expression was quantitated by flow cytometry. Results are from 3 separate experiments. Statistics, 2x vs 2x + hSiglec-5 Fc (10 μg), $p < 0.0005$.

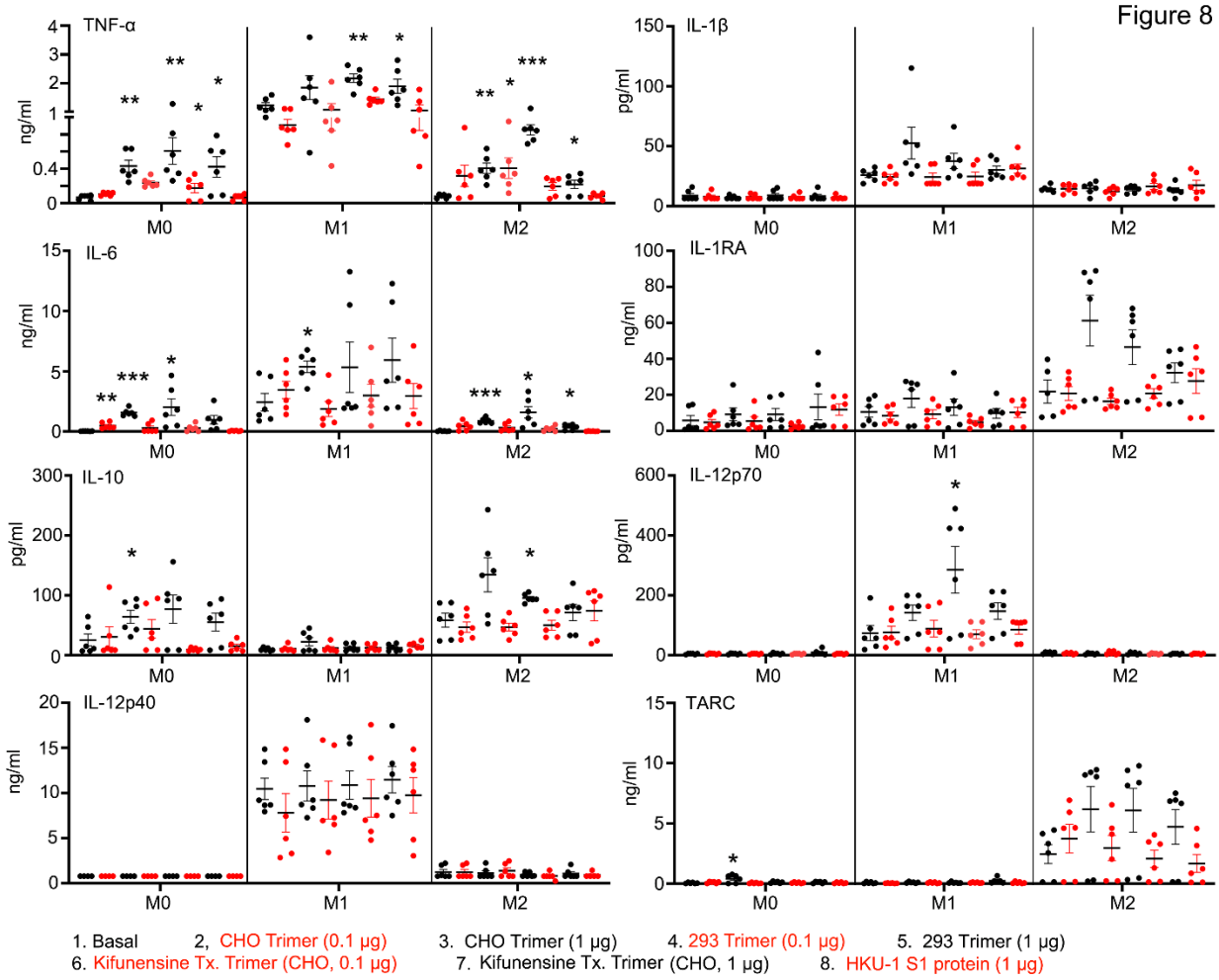

Figure 8. Macrophage cytokine profiles following exposure to different Spike proteins. Quantification of macrophage-associated cytokines in response to indicated Spike proteins. The graph shows the TNF-α, IL-1β, IL-6, IL-12p70, IL-12p40, and TARC quantification of M0, M1, or M2 Macrophage cultures following stimulation, or not, with SARS-CoV-2 Spike proteins derived from CHO cells (CHO Trimer; 0.1µg/ml or 1 µg/ml), or 293F cells (293 Trimer; 0.1 µg/ml or 1 µg/ml), or purified Spike protein from Kifunensine treated CHO cells (Kifunensine Tx. Trimer; 0.1 µg/ml or 1 µg/ml), or Human coronavirus HKU1 S1 protein (HKU-1 S1 protein; 1 µg/ml) for 48 hr. The error bars denote the mean ± SEM. Two-way ANOVA was used to compare treated samples to basal M0, M1, or M2 population (n = 6, *$p < 0.05$; **$p < 0.01$; ***$p < 0.001$).

Supplementary Material

Figure S1. Preparation of SARS-CoV-2 proteins.

Figure S2. Intranasal SARS-CoV-2 spike protein administration to K18-hACE2 mice.

Figure S3. Localization of Spike protein in the liver following intravenous administration.

Figure S4. Localization of SARS-CoV-2 Spike protein at other sites following intravenous injection and subcutaneous injection near the inguinal lymph node.

Video 1. Local Spike protein injection results in neutrophil recruitment in the cremaster muscle.

Video 2. Local injection of Spike proteins causes neutrophil fragmentation.

Video 3. Intravenously injected Spike protein outlines liver sinusoids and accumulates on Kupffer cells.

Video 4. Neutrophils undergo NETosis when plated on A549 cells in the presence of Spike protein.

Video 5. hSiglec-5 expressing HEK293 cells bind and endocytosis Spike protein.

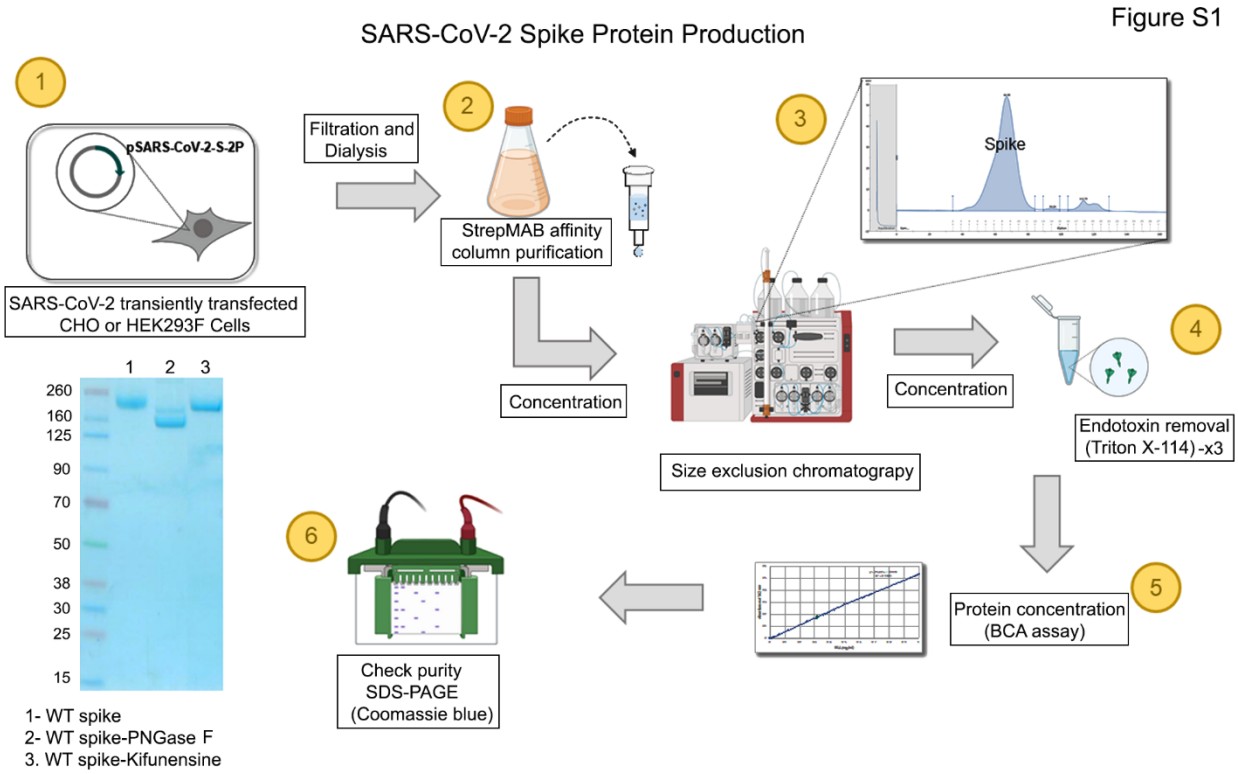

Figure S1. Preparation of SARS-CoV-2 proteins. Outline of recombinant proteins production and purification from cultured media of pSARS-CoV-2-S-2P transfected CHO or HEK293F cells.

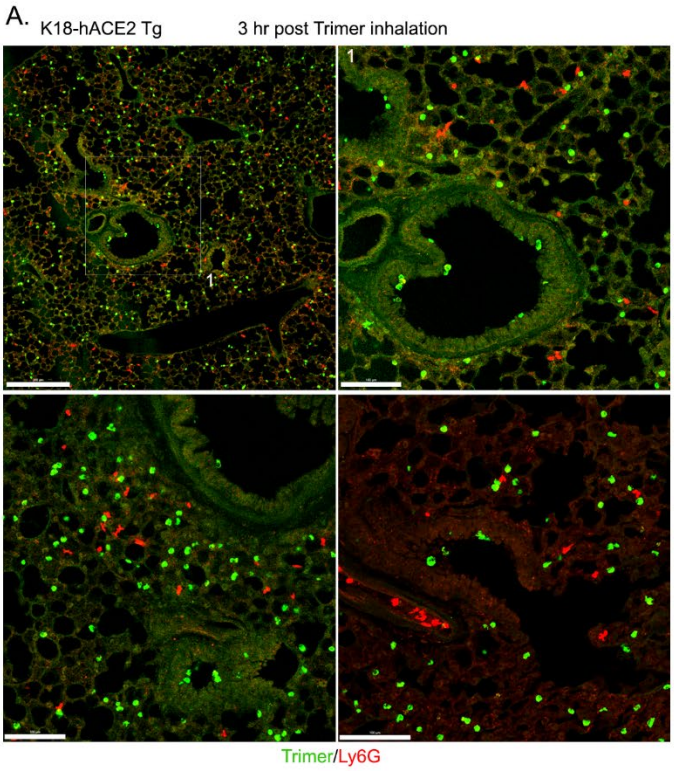

B. Figure S2

	JAX 664	JAX 034860 K18-hACE2
	Spike Trimer (CHO) (n=6)	Spike Trimer (CHO) (n=3)
Neutrophils	3.395 ± 0.916	3.507 ± 0.360
rMono	2.888 ± 0.759	6.830 ± 1.264 ***
iMono	3.565 ± 0.805	5.257 ± 0.828
AMac	77.467 ± 5.924	87.867 ± 2.609 **
iMac1	9.288 ± 3.234	6.577 ± 0.897
iMac2	13.583 ± 3.234	10.157 ± 0.645
iMac3	31.800 ± 7.223	11.477 ± 1.119 ***
Eosinophils	2.008 ± 0.539	3.803 ± 0.354
CD11b+DC	5.962 ± 1.136	10.497 ± 1.206 ***
CD11b-DC	3.702 ± 0.633	6.667 ± 0.750 **
NK&NKT	1.110 ± 0.176	3.623 ± 0.333 *
B	1.055 ± 0.196	2.403 ± 0.193
T	1.015 ± 0.360	2.710 ± 0.308

Figure S2. Intranasal SARS-CoV-2 administration to K18-hACE2 mice. (**A**) Representative confocal images of lung sections 3h post intranasal SARS-CoV-2 Spike protein (3 µg, green). Neutrophils immunostained with Ly6G. (**B**) SARS-CoV-2 Spike protein uptake by lung leukocytes 18 hr following intranasal inoculation. Flow cytometry results from analysis of leukocytes purified from the lungs of WT or K18-hACE2 mice. Data for JAX 664 mice same as shown in figure 2. K18-hACE2 leukocyte values significantly different from those from the JAX 664 mice are indicated, *p < 0.05; **p < 0.01; ***p < 0.001.

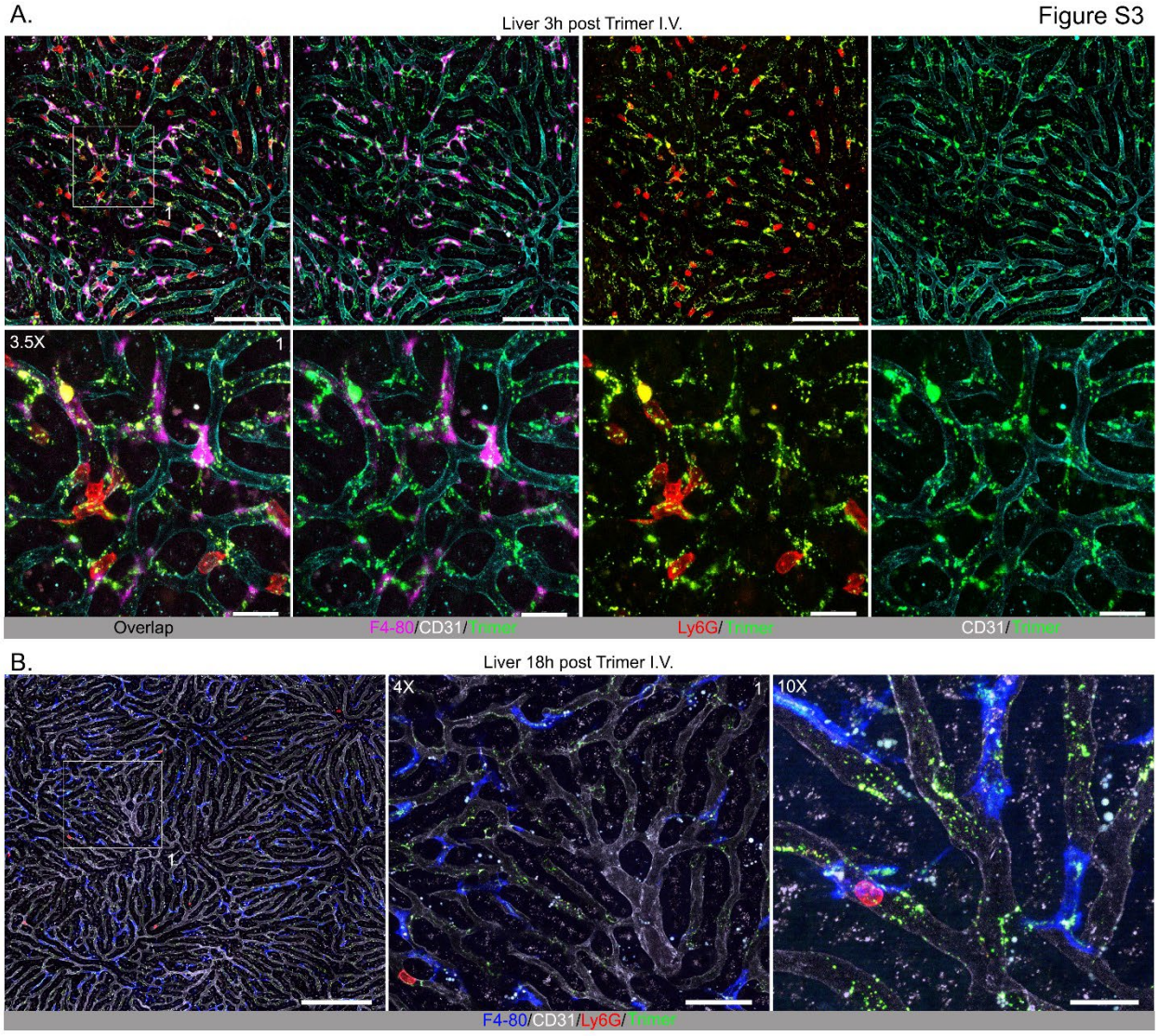

Figure S3. Localization of Spike protein in the liver following intravenous administration. **(A)** Confocal micrographs of the liver imaged at 3 hr post intravenous injection of SARS-CoV-2 spike (Trimer) protein. Spike protein (green), Kupffer cells (magenta, F4/80), and neutrophils (red, Ly6G) shown in liver sinusoid vasculature (cyan, CD31). Antibodies injected 0.3 hr before imaging. ROI-1 (box) (upper left) is enlarged (3.5 x magnification) in lower panels. Scale bars, 100 and 20 µm. (**B)** Confocal micrographs of liver imaged at 18 hr post intravenous injection of SARS-CoV-2 Spike protein. Spike protein (green), Kupffer cells (blue, F4/80), and neutrophils (red, Ly6G) are shown in liver sinusoid vasculature (white, CD31). Antibodies injected 0.3 hr before imaging. ROI-1 (box) (left) is enlarged in the middle panel (4 x magnification).

Enlarged image shows neutrophil contacting Spike protein bearing cells on liver sinusoid endothelium (10x magnification). Scale bars, 200, 50, and 20 µm.

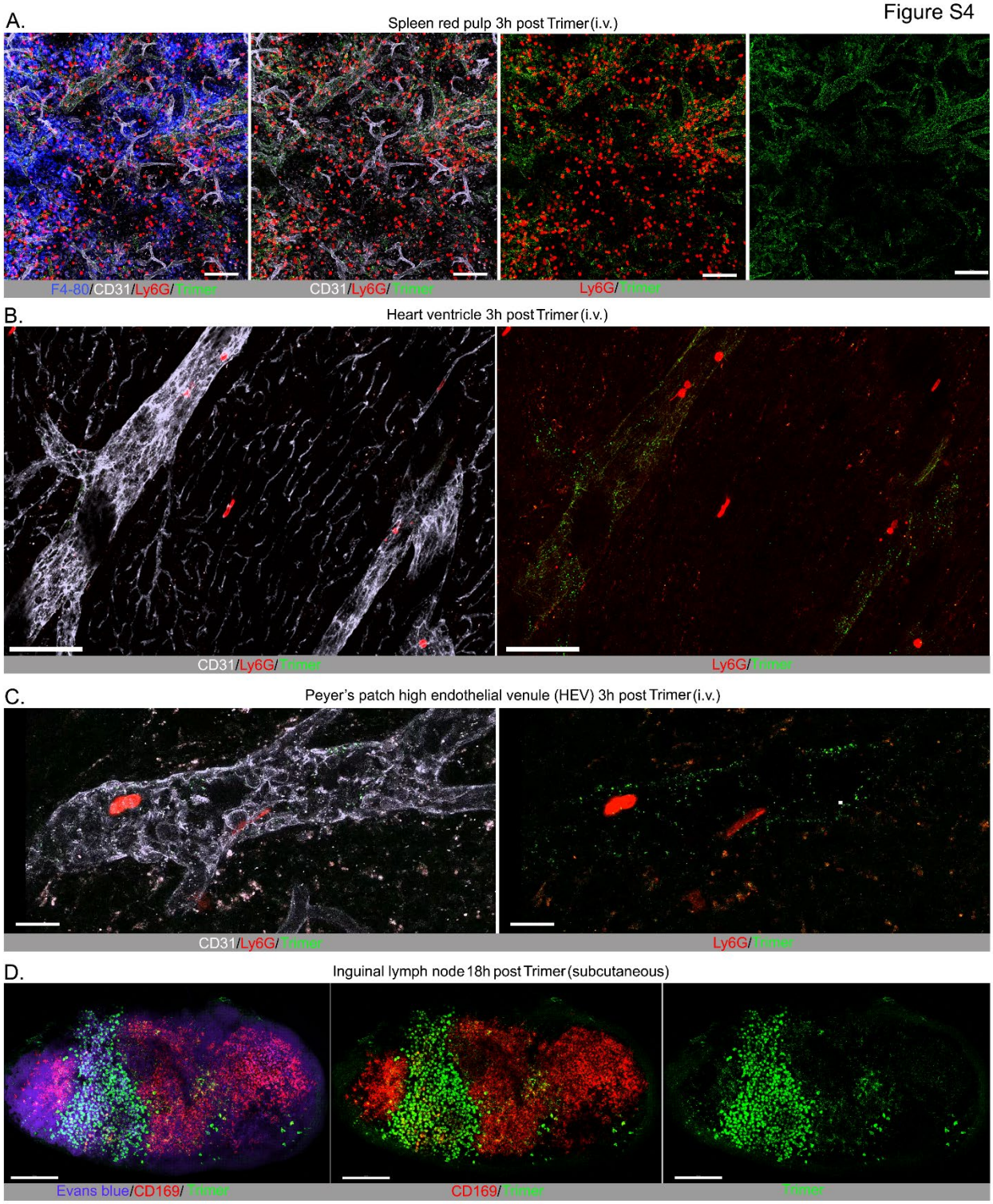

Figure S4. Localization of SARS-CoV-2 Spike protein at other sites following intravenous injection and subcutaneous injection near the inguinal lymph node. **(A)** Confocal micrographs of mouse spleen imaged 3 hr post intravenous injection of SARS-CoV-2 Spike (Trimer) protein. Spike protein (green), red pulp

macrophages (blue, F4/80), and neutrophils (red, Ly6G) visualized in spleen red pulp vasculature (cyan, CD31). Antibodies injected 1 hr before imaging. Scale bars, 100 µm. (**B)** Confocal micrographs of heart ventricle imaged 3 hr post intravenous injection of Spike protein. Spike protein (green) and neutrophils (red, Ly6G) localized in heart blood vessels (white, CD31). Antibodies injected 1 hr before imaging. Scale bars, 100 µm. (**C)** Confocal micrographs of Peyer's patch high endothelial venules (HEV) imaged at 3 hr post iv injection of Spike protein. Spike protein (green) and neutrophils (red, Ly6G) shown in HEV (white, CD31). Antibodies injected 0.5 hr before imaging. Scale bars, 20 µm. (**D)** Confocal micrographs of inguinal lymph node imaged at 18 hr post tail base injection of Spike protein. Spike protein (green) and subscapular sinus macrophages (red, CD169) shown. Subcapsular sinus defined via Evans blue (purple) signal. Antibodies and Evans blue injected 1 hr before imaging. Scale bars, 200 µm.

Video Legends.

Video 1. Local Spike protein injection results in neutrophil recruitment in the cremaster muscle. Confocal intravital microscopy movie shows neutrophils (green), platelets (red), endothelium (blue) immunostained with Alexa Fluor 488-Gr1, DyLight 649-GP1bβ, and Alexa Fluor 555-CD31 monoclonal antibodies, respectively. Intrascrotal injection of PBS or Spike protein (5 µg) 3-4 hours prior to imaging. The first sequence spans a ~60 min (PBS) while the second sequence spans a ~45 min (Spike) imaging period. Images were captured at ~1 frame per 30s with ~100X magnification. Time counter is hour:minute:second.

Video 2. Local injection of Spike proteins causes neutrophil fragmentation. Confocal intravital microscopy movie shows neutrophils (green), platelets (red), endothelium (blue) immunostained with Alexa Fluor 488-Gr1, Dylight 649-GP1bβ, and Alexa Fluor 555-CD31 monoclonal antibodies, respectively. Intrascrotal injection of Il-1β or Il-1β plus 5 µg Spike protein ~20 hours prior to imaging. Both sequences span a 20 min period. Images were captured at ~1 frame per 30s with ~100 x magnification. Time counter is hour:minute:second.

Video 3. Intravenously injected Spike protein outlines liver sinusoids and accumulates on Kupffer cells. The liver imaging was taken at three different time points; from 20 min to 1hr, from 1hr 10 min to 1hr 15 min, and from 1hr 25 min to 46 min after SARS-CoV-2 spike protein (green, Alexa Fluor 488) injection. An image sequence of a 12 µm z-projection was acquired with 40× lens as scanning speed of 11.05 sec between frames. Kupffer cells (magenta, F4/80), and neutrophils (red, Ly6G) in liver sinusoid vasculature (cyan, CD31) were visualized with antibody injection into tail vein at 30 min prior to imaging. The scale bar represents 20 µm. Time counter is hour:minute:second.

Video 4. Neutrophils undergo NETosis when plated on A549 cells in the presence of Spike protein. A549 cells were plated on chamber slide 48 hr before trimer treatment. SARS-CoV-2 spike trimer (green) was added to A549 cell culture 24 hr before neutrophil seeding. Purified human neutrophils stained with Hoechst (cyan) and were seeded on A549 cells in propidium iodide (PI, 1 µg/ml) containing culture media. NETosis of neutrophils were detected by exposed DNA (red, PI). An image sequence of a 20 µm z-projection was acquired with 40× lens at a scanning speed 1 frame /10 min over 5 hours. Regions of interest

(Box A and B) demonstrate a typical NETosis of neutrophil contacting on trimer bearing A549 cell were enlarged in second part of video. Scale bars, 30 and 10 μm. Time banner, hour:minute:second.

Video 5. hSiglec-5 expressing HEK293 cells bind and endocytosis Spike protein. Individually established stable-transfected cells expressing Siglec-5-GFP or ACE2-OFP were plated in the same chamber slide with non-transfection cells. After overnight culture SARS-CoV-2 spike protein (1 μg/ml) was overlaid for 1 hr before imaging. An image sequence of a 3 μm z-projection was acquired with 40× lens at a scanning speed of 23 sec between frames. Signals visualized as SARS-CoV-2 spike trimer (blue), Siglec-5-GFP (green), ACE2-OFP (red), and non-transfected HEK293 cells (gray). The scale bar represents 20 μm. Time counter is hour:minute:second.

1060 **Reagent Table**

Designation	Catalog Number	SOURCE	IDENTIFIER
Cell line			
FreeStyle™ CHO-S Cells	R80007	ThermoFisher Scientific	
FreeStyle™ 293-F Cells	R79007	ThermoFisher Scientific	
293T	CRL-3216™	ATCC	
293 [HEK-293]	CRL-1573™	ATCC	
A549	CRM-CCL-185™	ATCC	
Mice			
C57BL/6J	Jax stock 000664	Jackson Lab.	IMSR_JAX:000664
K18-hACE2 (B6.Cg- Tg(K18- ACE2) 2Prlmn/J)	Jax stock 034860	Jackson Lab.	IMSR_JAX:034860
Antibodies			
PerCP-Cy™5.5 Rat Anti-Mouse Ly6G	560602	BD Biosciences	RRID : AB_1727563
PE-Cy™7 Rat Anti-Mouse Ly6G	560601	BD Biosciences	RRID: AB_1727562
PE Rat Anti-Mouse I-A/I-E	557000	BD Biosciences	RRID: AB_396546
PE/Cyanine7 anti-mouse CD24 Antibody	101822	BioLegend	RRID: AB_756048
PerCP/Cyanine5.5 anti-mouse CD24 Antibody	101824	BioLegend	RRID: AB_1595491
Alexa Fluor® 647 anti-mouse CD64 (FcγRI) Antibody	139322	BioLegend	RRID: AB_2566561
Alexa Fluor® 488 anti-mouse CD31 Antibody	102414	BioLegend	RRID: AB_493408
Alexa Fluor® 594 anti-mouse CD31 Antibody	102432	BioLegend	RRID: AB_2617017
APC-Cy™7 Rat Anti-Mouse Siglec-F	565527	BD Biosciences	RRID: AB_2732831
PE anti-mouse CD170 (Siglec-F) Antibody	552126	BD Biosciences	RRID: AB_394341
Alexa Fluor® 647 Rat Anti-Mouse Siglec-F	562680	BD Biosciences	RRID: AB_2687570
BV421 Rat Anti-Mouse Ly6C	562727	BD Biosciences	RRID: AB_2737748
Brilliant Violet 650™ anti-mouse/human CD11b Antibody	101259	BioLegend	RRID: AB_2566568
Brilliant Violet 711™ anti-mouse CD45 Antibody	103147	BioLegend	RRID: AB_2564383
Brilliant Violet 785™ anti-mouse CD11c	117336	BioLegend	RRID: AB_2565268

1061

PE/Dazzle™ 594 anti-mouse CD19 Antibody	115554	BioLegend	RRID: AB_2564001
Brilliant Violet 421™ anti-mouse F4/80 Antibody	123137	BioLegend	RRID: AB_2563102
PE anti-mouse CD169 (Siglec-1) Antibody	142404	BioLegend	RRID:AB_10915697
PE anti-human CD16 Antibody	360704	BioLegend	RRID: AB_2562749
PE/Cyanine7 anti-human CD56 (NCAM) Antibody	362510	BioLegend	RRID: AB_2563927
APC Mouse Anti-Human CD4	551980	BD Bioscience	RRID: AB_398521
APC/Cyanine7 anti-human CD8a Antibody	301015	BioLegend	RRID: AB_314134
Brilliant Violet 421™ anti-human HLA-DR Antibody	307635	BioLegend	RRID: AB_2561831
Brilliant Violet 650™ anti-human CD14 Antibody	301836	BioLegend	RRID: AB_2563799
PerCP-Cy™5.5 Mouse Anti-Human CD14	550787	BD Bioscience	RRID: AB_393884
V500 Mouse Anti-Human CD14	561391	BD Bioscience	RRID: AB_10611856
Brilliant Violet 711™ anti-human CD20 Antibody	302341	BioLegend	RRID: AB_2562602
PE/Cyanine7 anti-human CD20 Antibody	302312	BioLegend	RRID: AB_314260
Alexa Fluor® 700 anti-human CD20 Antibody	302322	BioLegend	RRID: AB_493753
PE anti-human CD123 Antibody	306006	BioLegend	RRID: AB_314580
APC/Cyanine7 anti-human CD15 (SSEA-1) Antibody	323048	BioLegend	RRID: AB_2750190
APC anti-human CD66b Antibody	305118	BioLegend	RRID: AB_2566607
Brilliant Violet 421™ anti-human CD11c Antibody	337226	BioLegend	RRID: AB_2564485
BD Pharmingen™ PerCP-Cy™5.5 Mouse Anti-Human CD3	552852	BD Biosciences	RRID: AB_394493
PE Mouse Anti-Human CD22	562859	BD Bioscience	RRID: AB_2737845
APC anti-human CD170 (Siglec-5) Antibody	352005	BioLegend	RRID: AB_2564262
APC anti-human Siglec-8 Antibody	347106	BioLegend	RRID: AB_2561402
Alexa Fluor® 647 anti-mouse CD169 (Siglec-1) Antibody	142408	BioLegend	RRID: AB_2563621

Human Siglec-8 Antibody	MAB7975	R & D Systems	
Human Siglec-8 PE-conjugated Antibody	FAB7975P	R & D Systems	RRID: AB_2905537
Human Siglec-1/CD169 Alexa Fluor® 647-conjugated Antibody	FAB5197R-100UG	R & D Systems	RRID: AB_2905550
Human ACE-2 Alexa Fluor® 647-conjugated Antibody	FAB9332R-100UG	R & D Systems	
Human Siglec-8 Alexa Fluor® 750-conjugated antibody	FAB7975S-100UG	R & D Systems	
Human ACE-2 Alexa Fluor® 405-conjugated Antibody	FAB9332V-100UG	R & D Systems	
Human/Mouse/Rat/Hamster ACE-2 Antibody	AF933	R & D Systems	RRID: AB_355722
Mouse ACE-2 Antibody	AF3437	R & D Systems	RRID: AB_2223140
SARS-CoV-2 (2019-nCoV) Spike Neutralizing Antibody, Rabbit Mab	40592-R001	SinoBiological	RRID: AB_2857936
Rat IgG derivative against the GPIbβ subunit of the murine platelet/megakaryocyte-specific GPIb-V-IX complex antibody	X647	Emfret	RRID: AB_2861336
Mouse LYVE-1 Antibody	MAB2125	R & D Systems	RRID: AB_2138528
PE anti-mouse Podoplanin Antibody	127408	BioLegend	RRID: AB_2161928
Buffer and chemicals			
LIVE/DEAD™ Fixable Aqua Dead Cell Stain Kit	L34966	Thermo Fisher Scientific	
Evans Blue	E2129-10G	Sigma-Aldrich	
Propidium Iodide (PI)	P4864-10ML	Sigma-Aldrich	
FluoSpheres™ NeutrAvidin™-Labeled Microspheres, 0.2 µm, yellow-green fluorescent (505/515), 1% solids	F8774	Thermo Fisher Scientific Inc.	
2M MgCl2	340-034-721	Quality Biological Inc.	
2M CaCl2	351-130-721	Quality Biological Inc.	
HBSS wo Ca2+&Mg2+	14175-095	Thermo Fisher Scientific Inc.	
Albumin, Bovine Serum, Fraction V, Fatty Acid-Poor, Endotoxin-Free	126579-100GM	Sigma-Aldrich	

5M NaCl	351-036-101	Quality Biological Inc.	
2M Tris-HCl, pH8.0	351-092-101	Quality Biological Inc.	
1X PBS wo Ca2+ & Mg2+	114-058-101	Quality Biological Inc.	
0.5M EDTA, pH8.0	351-027-101	Quality Biological Inc.	
Manganese (II) chloride tetrahydrate	63535-50G-F	Sigma-Aldrich	
Liberase™ TL(Thermolysin Low) Research Grade	5401020001	Roche Applied Science	
DNase I	10104159001	Roche Applied Science	
Cover glass	Cover glass – #4860-1D	Brain Research Laboratories	
Universal Mounting Frame AK-Set		PECON	
Opti-MEM™	31985070	Thermo Fisher Scientific Inc.	
RPMI 1640 Media	11875093	Thermo Fisher Scientific Inc.	
TransIT-293 Transfection Reagent	MIR 2704	Mirus Bio LLC	
Lenti-X™ Concentrator	631232	Takara Bio USA Inc.	
FreeStyle™ 293 Expression Medium	12338018	Thermo Fisher Scientific Inc.	
FreeStyle™ CHO Expression Medium	12651014	Thermo Fisher Scientific Inc.	
Plasmids			
SIGLEC5 (NM_003830) Human Tagged ORF Clone	RC206610	Origene	
SIGLEC5 (NM_003830) Human Tagged ORF Clone	RG206610	Origene	
Human Siglec-8 (NP_055257) VersaClone cDNA	RDC1496	Origene	
SARS-CoV-2 Spike-S			
HIV-1 NL4-3 Gag-iGFP ΔEnv	12455	NIH AIDS Reagent Program	

Human Coronavirus spike glycoprotein Gene ORF cDNA clone expression plasmid(Codon Optimized) HCoV-HKU1	VG40021- UT	SinoBiological	
Human coronavirus(HCoV-229E) Spike Gene ORF cDNA clone expression plasmid(Codon Optimized) HCoV-229E	VG40605- UT	SinoBiological	
ACE2 cDNA ORF Clone, Human, C-OFPSpark® tag	HG10108-ACR	SinoBiological	
pCMV-dR8.2 dvpr	8455	Addgene	
pLentipuro3 TO V5-GW EGFP-Firefly Luciferase	119816	Addgene	
Recombinant Protein			
ACE2 Protein, Human, Recombinant (mFc Tag)	10108-H05H	SinoBiological	
Human coronavirus HKU1 (isolate N5) (HCoV-HKU1) Spike/S1 Protein (S1 Subunit, His Tag)	40602-V08H	SinoBiological	
Human coronavirus (HCoV-229E) Spike Protein (S1+S2 ECD, His Tag)	40605-V08B	SinoBiological	
SIGLEC5 Protein, Human, Recombinant (hFc Tag)	11798-H02H	SinoBiological	
Recombinant Mouse Siglec-F Fc Chimera Protein, CF	1706-SF-050	R & D Systems	
Recombinant Human Siglec-8 Fc Chimera Protein, CF	9045-SL-050	R & D Systems	